Determination of Process Parameters for the Manufacturing of Thermoplastic Composite Cones Using Automated Fiber Placement

Xiao Cai

A Thesis

In

The Department

Of

Mechanical and Industrial Engineering

Presented in Partial Fulfillment of the Requirements

For the Degree of

Master of Applied Science (Mechanical Engineering) at

Concordia University

Montreal, Quebec, Canada

June 2012

CONCORDIA UNIVERSITY

SCHOOL OF GRADUATE STUDIES

This is to certify that the thesis prepared,

By: **Xiao Cai**

Entitled: "**Determination of Process Parameters for the Manufacturing of**

Thermoplastic Composite Cones Using Automated Fiber Placement"

and submitted in partial fulfillment of the requirements for the degree of

Master of Applied Science (Mechanical Engineering)

complies with the regulations of this University and meets the accepted standards with respect to originality and quality.

Signed by the Final Examining Committee:

_____Chair
Dr. I. Stiharu

_____Examiner
Dr. M. Pugh

_____Examiner
Dr. M. Nokken   External
Building, Civil and Environmental Engineering

_____Supervisor
Dr. S. V. Hoa

_____Co-Supervisor
Dr. M. Hojjati

Approved by   _____
Dr. S. Narayanswamy, MASc Program Director
Department of Mechanical and Industrial Engineering

_____
Dean Robin Drew
Faculty of Engineering & Computer Science

Date: _____

Abstract

Determination of Process Parameters for the Manufacturing of Thermoplastic Composite

Cones Using Automated Fiber Placement

Xiao Cai

In-situ fiber placement, in combination with automated tape laying and filament winding, is the key to high-volume production of large-scale composite aerostructures ranging from simple flat plates, to panels with mild curvatures, to complex three-dimensional surfaces, promising reliable, consistent and cost-effective fabrication. However, manufacturing cost, slit tape quality, lack of knowledge and experience of the in-situ consolidation fiber placement process are major barriers preventing aircraft manufacturer from implementing this unique processing technique.

This dissertation aims to gain knowledge and experience of in-situ consolidation fiber placement by identifying and resolving four technical issues associated with the manufacturing of thermoplastic composite tailbooms. The first study demonstrates that the percentage of gap/lap and the angular deviation of fiber orientation can be controlled by dividing a single tool surface to multiple and equal sections. The second study shows that the interlaminar defects have minimal effects on the mechanical properties of autoclave molded thermoplastic composite laminates. The third study predicates a set of optimum processing parameters for manufacturing tailboom demonstration articles using automated fiber placement. The last study suggests that the in-situ consolidation fiber placement process needs to be improved to lower the micro-size void content and minimize the process induced warpage.

Acknowledgement

Table of Contents

List of Figures

List of Tables

CHAPTER 1   Introduction

Composite materials have been extensively employed in the primary and secondary structures of military and commercial aircrafts along with developing and maturing technologies of both materials and material processing. In the past 25 years, the technical advances in the automated manufacturing of composites have increasingly attracted the interests of the aerospace industry. Indeed, the flexibility of the process allows the fabrication of highly contoured composite parts with minimum machine setup. For instance, the Boeing 787 Dreamliner is composed of a total composite of 50 % by weight [1], including the integration of an all composite fuselage, wings and tail shown in Figure 1.1. The Airbus A350 XWB pushes the envelope to a total composite of 53 % by weight [2]. Heretofore, the vast majority of composite materials for aerospace were based on thermoset materials, and only a small amount of thermoplastic composite parts on the Airbus A340 and A380 included the fixed wing leading edge, keel beams and other components [3].
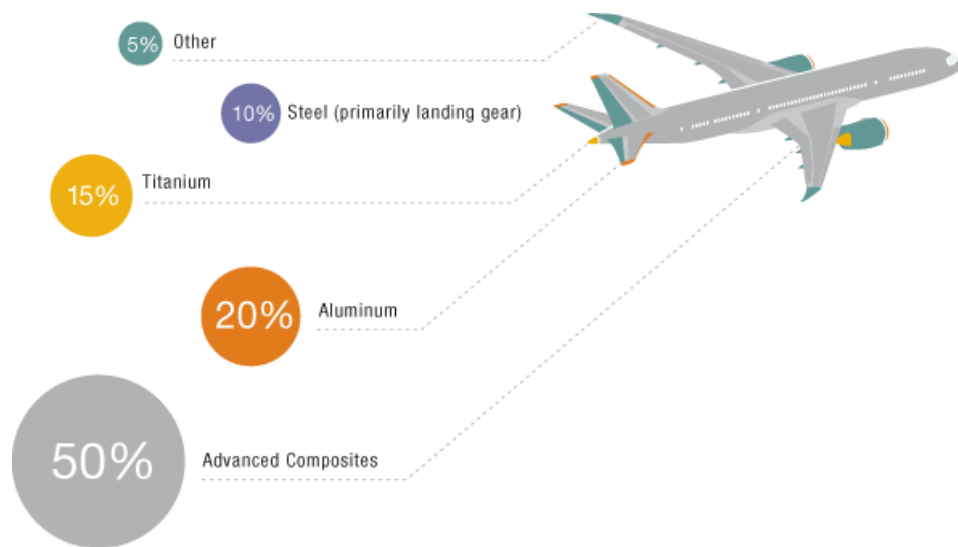
Figure 1.1 Boeing 787 Dreamliner composite profile [4]

The aerospace industry has focused on the applications of thermoset composites for three main reasons [3]. First, a comprehensive knowledge database for thermoset materials has been established through years of research and practice. Second, substantial investments in thermoset composites have been made for design tools, material properties databases, capital equipment, employee training, and test methodologies. Third, conversion to alternate materials or processes leads to reinvestment and requalification costs, as well as retraining of engineering and manufacturing personnel.

In comparison to thermoset composites, thermoplastic composites have recently received more attention from the aerospace industry due to their unique characteristics [3]. From a material standpoint, thermoplastic composites are melt-processable polymers that provide a versatile process. They have a nearly infinite shelf life that reduces handling and shipping costs compared to thermoset composites. Moreover, thermoplastic composites are much tougher than comparable thermoset composites, which results in better resistance to impact and crack initiation and propagation [5]. They also exhibit excellent chemical resistance to hydraulic oils, aviation fuels, and chemical solvents [5]. Furthermore, thermoplastic composites offer substantial reduction in flammability, smoke and toxicity [5]. From a processing standpoint, thermoplastic composites and their associated processing innovations, such as automated fiber placement (AFP), eliminate the need for autoclave processing, which lowers capital cost, floor space requirements and processing bottleneck issues. Last but not least, thermoplastic composites can be fully recycled at the end of their life.

In 1994, a group of researchers from Bell Helicopter Textron Inc. (BHTI) and Automated Dynamics (also known as ADC) demonstrated that a thermoplastic composite

tailboom, using the in-situ consolidation fiber placement process, for the Bell OH-58 Kiowa tailboom is a viable low-cost alternative to aluminum or thermoset composite construction [6]. A 6-ft long afterward section of the tailboom was fabricated by ADC and tested by BHTI. As an extension of previous work, Bell Helicopter Textron Canada Ltd. (BHTCL) initiated a research project in 2008 in collaboration with five industrial and academic partners from Canada to carry out the manufacturing feasibility study of fiber-placed thermoplastic composite (AS4/APC-2 by Cytec Engineered Materials) tailbooms for the Bell 407 helicopter as shown in Figure 1.2. A typical tailboom consists of a truncated conical shell and many fairlead support frames mounted along the axial direction of the conical shell. The tailboom is considered to be a primary structure, which provides the support for the tail rotor and produces a counterbalancing torque to offset the torque produced by the main rotor. A conical section that is similar to a forward section of current aluminum tailbooms was selected for this study.

Aluminum tailbooms currently used on light-medium helicopters are structurally efficient and cost-effective. Advanced composite materials offer advantages over aluminum such as excellent corrosion resistance and superior stiffness properties. However, the manufacturing cost of composites is much higher than that of aluminum, and the structural integrity requirements, particularly damage tolerance, are demanding. The in-situ consolidation fiber placement process using a carbon fiber/thermoplastic material system has been studied to overcome those barriers. Thermoplastics offer a number of service advantages including tolerance resistance, service temperatures, and corrosion resistance. These advantages, in combination with the low-cost in situ

16

consolidation process, make thermoplastic composites attractive from both a service and a production standpoint.

Figure 1.2 Photo of Bell 407 helicopter (photo courtesy of Bell Helicopter Textron Candada)

In order to make the thermoplastic composite tailboom viable for production, the total cost, including life-cycle costs, has to be less expensive than that for the aluminum tailboom. The capability of laying down slit tapes on an inner mold line (IML) surface without needing to consolidate using an autoclave, as well as improved assembly time through the use of IML tooling, has provided the means to fabricate an inexpensive tailboom. Moreover, this fabrication process allows the fibers to be placed in any direction circumferentially around the cone so that a complete monocoque shell could be built without a splice. The monolithic tailboom reduces the assembly time of joints and fasteners significantly but sacrifices the accessibility to internal components during periodic servicing and inspection.

There are two major advantages to the in-situ consolidation fiber placement process. The first is that this process offers a seamless structure; the second is that the structure is constructed on the IML surface. The majority of the costs associated with the manufacturing of the tailboom are assembly costs which are dominated by rivet and fastener installation. The internal bulkheads, which are assembled on a tooling fixture matched to the IML surface of the tailboom, are easily mated to the monocoque of the tailboom. This approach allows a close fit between the support frames and the tailboom skin, thus minimizing the manufacturing time to install the frames. However, the higher material costs offset the cost savings associated with assembly, resulting in essentially no cost reduction. However, the reduction in weight results in lower operational costs.

However, this process still has significant barriers to overcome before it can be widely used in the manufacturing of primary aerostructures. Apart from costs, the main issue is how to fabricate high quality laminates. The reasons can be due to slit tape quality and lack of knowledge and experience of the in-situ consolidation fiber placement process. The slit tape quality relies on the manufacturing technique implemented by the material supplier. Unlikely, the knowledge and experience how to fabricate sound composite structures with a set of well-defined process parameters must be acquired through researching and practicing. It must be pointed out that the word "process parameter" is a broad concept, which includes fiber path design, path generation algorithm, temperature and pressure settings, tooling, and etc. To realize the benefits of the in-situ consolidation technique, it is crucial to identify process related issues and resolve them at the early stage of the process development with the help of experts who are familiar to the field of composite material processing. In the presented study, four

technical challenges associated with the in-situ consolidation fiber placement process that are identified by the research team have to be resolved prior to the production phase.

(1)   The first challenge is to propose a strategy for laying down slit tapes on the IML surface such that the percentage of gaps and laps and the deviation of fiber orientation would be balanced, and compaction load distribution could be uniform. Placing slit tapes on a highly contoured surface with a straight and rigid compaction roller leads to a non-uniform pressure distribution between the incoming tape and the substrate. The effective contact length of the IML surface and the compaction roller is shorter than the width of the slit tapes so that the void content may be higher at the two free edges than in the middle.

(2)   The second challenge is to characterize the effects of gaps and laps embedded in a thermoplastic composite laminate on its mechanical properties such as tensile, compression, and shear properties. The tapering of the tailboom causes a decrease in material requirements along the tailboom axis due to the reducing cross-sectional area. Laying up slit tapes on a truncated conical surface leads to a geometric fit-up problem, also called "gaps and laps".

(3)   The third challenge is to find the optimum process condition for processing AS4/APC-2 on the fiber placement work cell. The resulting quality of fiber placed laminates strongly depends on the processing parameters, for example heat flux, lay-down speed, and consolidation pressure. The average effect of these process parameters and their interactions provide insight into finding an optimal combination for the in-situ fiber placement process.

(4)   The last challenge is to characterize the environmental influences on the bond strength between fiber placed skin and autoclave molded frame by diffusion welding. Airframe structures in service are usually subjected to different environmental conditions such as water, hydraulic fluid, and jet fuel. Long-term exposure to these liquids may deteriorate the bond strength of those made of composites and add extra weight to the structures.

This dissertation aims to resolve the challenges associated with the manufacturing of thermoplastic composite tailbooms with the in-situ consolidation fiber placement process. The core chapters of the dissertation are structured as follows: (1) CHAPTER 3 presents a theoretical study of fiber path planning; (2) CHAPTER 4 presents an experimental investigation of the influences of laps and gaps on the mechanical properties of a thermoplastic laminate; (3) CHAPTER 5 presents a study of the optimization of process parameters for the in-situ consolidation process; (5) CHAPTER 6 presents an experimental investigation of the effects of the liquid environment on the single-lap joint strength.

CHAPTER 2   Literature Review

A literature review was performed to introduce the in-situ fiber placement process and to investigate the technical issues associated with the process. Particular issues of interest for this review include planning of fiber path, influence of gaps and laps, moisture absorption of fiber placed thermoplastic composites, and process optimization for in-situ fiber placement. The review includes journal articles, handbooks, and other reference books relative to the objectives of this effort.

2.1   Introduction of In-Situ Fiber Placement

The development of the fiber placement process offers possibilities to manufacture large-scale composite aerostructures ranging from simple flat plates, to panels with mild curvatures, to complex three-dimensional surfaces at lower cost in comparison to traditional processing techniques. The fiber placement technique offers the capability of precise fiber orientation control and hence strength tailoring. Fiber placement manufacturing typically produces 2 % to 15 % scrap, as compared to 50 % to 100 % scrap for the traditional technique of draping resin impregnated cloth by hand layup. Additionally, the process of fiber placement offers the assurance of repeatability that is not possible with hand layup techniques on free form surfaces. Along with automated tape laying and filament winding, in-situ fiber placement is the key to high-volume production of composite structures, promising reliable, consistent and cost-effective fabrication.

As an example, the Automated Dynamics' in-situ fiber placement process is detailed in Figure 2.1. Prepreg tows that are stored in a creel system are fed with a controlled amount of tension through a series of precision guiding chutes of the

processing head to the contact point of the compaction roller and the previous ply. The amount of tension is usually low and is present to ensure fiber straightness rather than to emulate a filament winding process. A hot gas torch (HGT) is utilized to heat an inert gas to a set temperature. This heated gas is used to flood the contact point with a great amount of thermal energy, raising the temperature of the tows to their melting point. More importantly, the inert gas protects the tows from oxidative degradation during the bonding process [7, 8]. A compaction roller provides the necessary forces to achieve complete intimate contact across the tow interface, and the boundary pressure for compressing spatial voids as the processing head moves across the surface of the part. The consolidated tows then cool under ambient air temperature conditions. Proper compaction is required to prevent residual stresses, voids, and warping [9]. During the fiber placement process, the robot's end-effector must be oriented in such a way that the compaction roller pressure always acts normal to the tool surface. To continue laying the fibers in a different direction, the tows have to be cut. The robot manipulator is then moved to new starting position and the tows are fed by a servo motor. The whole process then repeats again until the completion of the part. More importantly, the processing parameters are carefully selected so that the tows are fully consolidated after being deposited and do not require any post-processing.
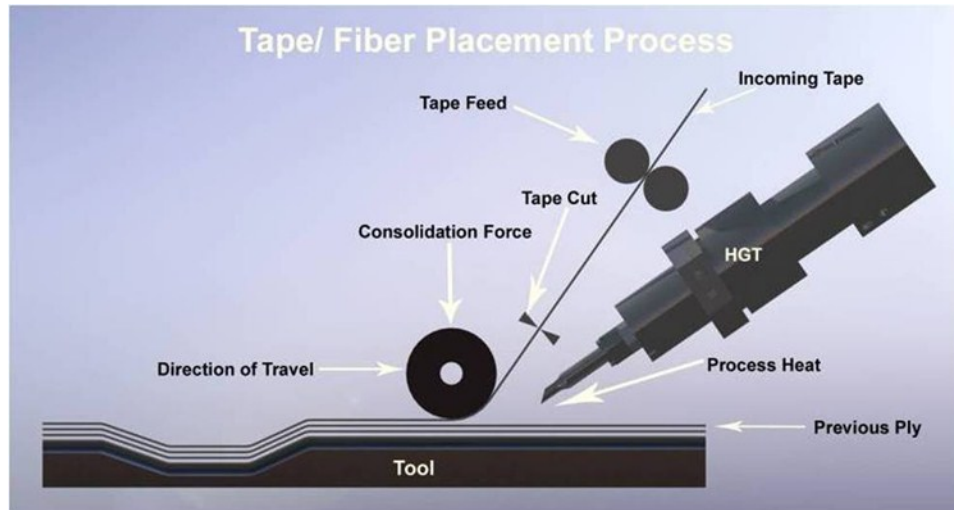
Figure 2.1 Illustration of fiber placement process (photo courtesy of Automated

Dynamics)

2.2   Planning of Fiber Path for Surface Coverage and Angular Deviation

A special challenge to the fiber placement process is the requirement to produce a

tailboom with a constant wall thickness and a minimal amount of gaps and overlaps

illustrated in Figure 2.2 [6]. The placement of slit tapes on the IML surface has to be

evaluated with respect to the surface geometry to determine fiber path planning based

upon the limitations of tooling, the percentage of gap and overlap, and the tolerance of

fiber orientation. Tessnow, Hutchins, Carlson, and Pasanen [6] propose four approaches

for placing slit tapes on a developed conical surface. They conclude that the optimum

fiber placement design is to repeat the pattern four times around the periphery of the

opened surface, for both 0° and ±45° fiber orientations. No gaps are allowed for the 0°

plies, and no overlaps are allowed for the ±45° plies. As a result, a series of triangular

laps or gaps are arranged along the length and circumference of the tailboom. Anderson

[10] shows that overlaps have less impact on the strength of fiber placed parts than gaps

based upon porosity analysis. Recently, Marsden, Fews, Oldroyd, and Yousefpour [11]

present an analysis of the percentage of overlap and the maximum deviation of fiber orientation for a $0°$ fiber placed ply. They point out that the fiber path design is optimized for weight, angular deviation, tow length, and machine run time. A well-considered plan for fiber placement can reduce the machine run time up to 25 %. Quinn [12] concludes that the current use of a metal compaction roller is not the optimal method of applying compaction force on a complex geometry during processing. However, it is the only compaction system commercially available in the market for the fiber placement system. The real challenge is to design a rigid roller which has close fit with the IML surface.
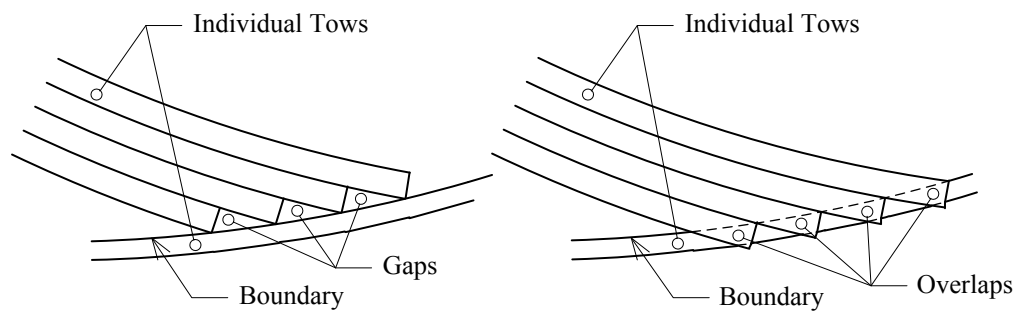
Figure 2.2 Illustration of gaps and laps on a ply

2.3   Influences of Process-Induced Defects on Mechanical Performance of Fiber Placed Laminate

During the fiber placement process, interlaminar defects like laps and gaps are the result of machine and human inaccuracies, as well as the inability of slit tapes to conform to complex geometries [13]. Failure to remove these defects by processing leads to permanent flaws in the resulting laminate. The use of narrow strips results in a large number of strip interfaces in fiber placed laminates which increases the probability of the occurrence of gapping and overlapping due to the in-plane waviness and the width

variance of fiber placed tows. The fiber placed tows exhibit in-plane waviness as the fibers tend to be slightly deviated from the planned trajectory when placed down in narrow strips [14]. Moreover, the width variance of slit tape may result in interlaminar defects at the strip interfaces. Gaps and laps also cause out-of-plane waviness in adjacent plies. Sawicki and Minguet [14] conclude that a fiber placed IM6/3501-6 laminate containing one 0.03 in wide overlap and gap has lower compression strength as compared to that without the defects. Anderson [10] suggests that AS4/APC-2 laminates with the interlaminar defects exhibit lower laminate strength than those without any defects owing to the increased porosity. Croft et al. [15] demonstrate that fiber placed thermoset composite laminates containing the aforementioned defects present a strength reduction of up to15 %. The impact of these defects on the mechanical performance of thermoplastic laminates has not been investigated yet.

2.4   Process Optimization for In-Situ Fiber Placement

One of the most important measures of quality in a fiber placed composite part is the bond strength that develops between each ply upon placement [16]. The bond strength governs the ability of the laminate to transfer interlaminar loads between individual plies as the material undergoes a complex thermal and pressure history, both of which affect the bond strength development. Heat flux, lay-down speed, and consolidation pressure are the principle controllable process variables which are known to influence thermal history and resulting laminate quality [17, 18]. Other process parameters which influence final material properties are nitrogen flow rate, tool temperature and roller temperature. These settings are fixed in the current study in the following ways: (1) the nitrogen flow rate is maintained at 70 SLPM possible to extend the life span of HGT; (2) the tool is not

heated due to the limitations on time and budget; and (3) the compaction roller is not heated because of the space limitation of the thermoplastic placement head. The in-situ consolidation fiber placement involves the concurrent use of both heat and pressure so that the tows bond at their interface. The two mechanisms that contribute to the strength development at the polymer–polymer interface in this process are the development of complete mechanical contact and the diffusion of polymer chains across those contacting surfaces [19-23].

2.5   Environmental Influences on Stiffened Thermoplastic Composite Structural Made Using Automated Fiber Placement

Two research programs conducted at the European Aeronautic Defence and Space Company (EADS) and the National Aeronautics and Space Administration (NASA) demonstrate that thermoplastic composite skin-stringer panels can be manufactured by embedding pre-consolidated thermoplastic stringers into an IML tool and then tape placing over them by diffusion welding for performance optimization and cost reduction [24, 25]. Thus, the skin-frame structure for the tailboom can be built with the in-situ consolidation fiber placement process in the same way as the skin-stringer structures. However, neither of them has published experimental data on the bond strength between a pre-consolidated and a fiber-placed thermoplastic composite laminate by diffusion welding or discussed the environmental effects on the jointed structure. In service, integrated composite structures may be subjected to different environmental conditions, for example water, hydraulic fluid, and aviation fuel. Many studies show that carbon- or glass-reinforced thermoset composites degrade by exposure to distilled water, sea water, hydraulic fluids, jet fuels, and anti-icing additives [26-28]. The degradation mechanisms

include the matrix plasticization and the fiber/matrix hydrolysis [29]. The loss of mechanical properties by plasticizing is recoverable by removing water moisture [29]. However, the loss of mechanical properties is irreversible when fiber/matrix hydrolysis occurs [29].

In contrast, thermoplastic composites exhibit excellent environmental resistance. In particular, APC-2 has outstanding chemical resistance and is extremely resistant to most organic and inorganic chemicals. It was reported that the tensile, compression strength, compression after impact and fatigue of such composites were not affected by moisture absorption, which was explained by low moisture uptake of the matrix material [30, 31].

In addition to the reduction in the mechanical performance, a weight gain can be observed due to moisture absorption. Many composites are hydrophilic absorbing as much as 5 % of water, which leads to an increase in the payload [29]. Unlike thermoset composites, thermoplastic composites exhibit low moisture absorption. The water absorption of compression molded AS4/PEEK laminate was 0.1 % after a 9-month immersion in distilled water at 50 °C [29]. The fiber placed composites, on the other hand, might exhibit higher moisture content than compression or autoclave molded ones owing to the presence of voids.

CHAPTER 3   Effects of Fiber Path Planning on Fiber Orientation and Compaction Roller Radius

The simulation of fiber placement in CATIA aims to find a strategy for laying slit tapes at two fiber orientations ($0°$ and $45°$) on a truncated conical surface prior to the fabrication of tailboom demonstration article. The fiber placement design must meet the tolerance requirements of fiber orientation and the percentage of laps. The number of divided sections from the conical surface and the minimum radius of the compaction roller were determined by analyzing the CATIA models. As the fiber path with a constant helical angle was not able to be generated by any inherent function from CATIA V5, a mathematical model describing the trajectory of an initial fiber path was developed. The initial path on the conical support surface was defined by a series of points obtained from the mathematic model. The adjacent path was offset along the conical support surface a distance of a single tow-width in a perpendicular direction from the initial path. Since the angular deviation and the minimum roller radius increases with increasing the offset distance of a fiber path from the initial path, dividing a conical surface into two or more identical sections is beneficial for controlling the angular deviation [14]. However, the more sections the conical surface is divided into, the more gaps and laps the fiber placed laminates contain. It is essential to understand the relationships between the number of sections and the angle of deviation, the percentage of overlapped area, and the minimum roller radius.

Figure 3.1 Illustration of gaps highlighted in white between two sections on a 0° ply

(photo courtesy of the National Research Council Canada)

3.1 Mathematical Model of Initial Fiber Path

As shown in Figure 3.2, a Cartesian coordinate system obeying the right-hand rule is attached to the conical surface. The revolving axis of the conical surface is taken as the z-axis and the xoy-plane passes through the larger end of the cone. Let the fiber path start from x-axis. In this coordinate system, the equation of a conical surface is

$$\begin{cases} x = r(z)\cos(\phi(z)) \\ y = r(z)\sin(\phi(z)) \\ \quad z = z \end{cases} \tag{3.1}$$

where $r(z)$ is the radius of the conical surface, $\phi(z)$ is the angular parameter, z is parametric variable. Thus, the parametric function of the conical surface can be written as

$$\boldsymbol{r}_s = \left\{ r(z)\cos(\phi(z)), r(z)\sin(\phi(z)), z \right\} \tag{3.2}$$

29
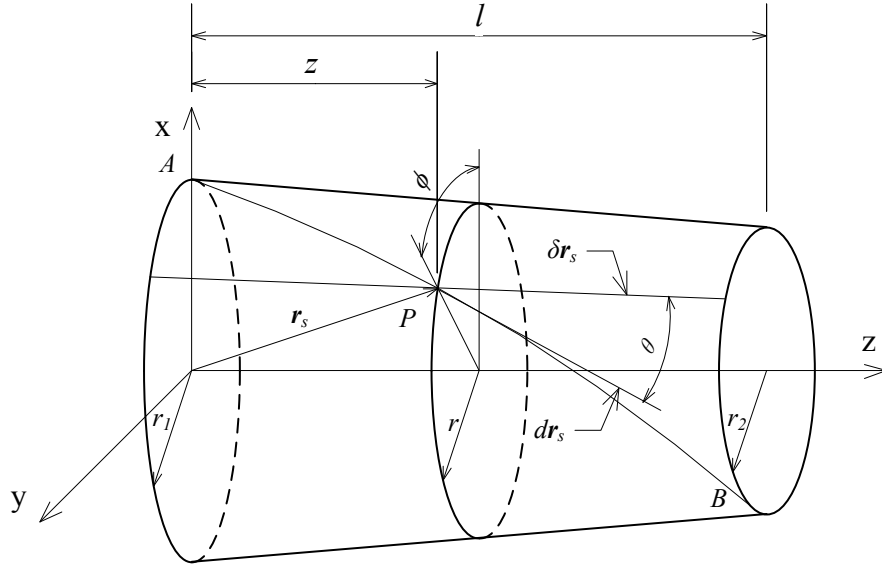
Figure 3.2 Cartesian coordinate of a conical surface

In order to obtain the coefficients of the first fundamental form, the following partial derivative of the function with respect to z and $\phi(z)$ should be calculated

$$\frac{dr_s}{dz} = r_{s,z} = \{r'(z)\cos\phi, r'(z)\sin\phi, 1\} \tag{3.3}$$

and

$$\frac{dr_s}{d\phi} = r_{s,\phi} = \{-r(z)\sin\phi, r(z)\cos\phi, 0\} \tag{3.4}$$

The coefficients of the first fundamental form can be obtained as

$$E = r_{s,z} \cdot r_{s,z} = 1 + r'^2 \tag{3.5}$$

$$F = r_{s,z} \cdot r_{s,\phi} = 0 \tag{3.6}$$

$$G = r_{s,\phi} \cdot r_{s,\phi} = r^2 \tag{3.7}$$

The tangent vector of the planar profile of the conical surface can be expressed as

$$\delta r_s = r_{s,z} dz \tag{3.8}$$

30

Let dr_s be the tangent vector of a point on the fiber path with a constant angle to the vector δr_s, dr_s can be defined as

$$dr_s = r_{s,z}dz + r_{s,\phi}d\phi \tag{3.9}$$

By using the definition of the dot product of two vectors, the helical angle can be expressed as

$$\cos^2 \theta(z) = \left(\frac{dr_s \cdot \delta r_s}{|dr_s||\delta r_s|}\right)^2 = \frac{Edz^2}{Edz^2 + Gd\phi^2} \tag{3.10}$$

where θ is the helical angle of the fiber path. By separating the variables of z and $\phi(z)$, the above equation becomes

$$dz^2\left(\frac{E}{\cos^2 \theta(z)} - E\right) = Gd\phi^2 \tag{3.11}$$

By substituting the coefficients of the first fundamental form into the above equation, the equation can be rewritten as

$$d\phi = \sqrt{\frac{(r'^2 + 1)}{\cos^2 \theta(z)} - (r'^2 + 1)} \frac{1}{r}dz \tag{3.12}$$

or

$$\phi = \int \sqrt{\frac{(r'^2 + 1)}{\cos^2 \theta(z)} - (r'^2 + 1)} \frac{1}{r}dz \tag{3.13}$$

where

$$r = r_1 - \frac{z}{l}(r_1 - r_2) \tag{3.14}$$

and

31

$$\frac{dr}{dz} = -\frac{1}{l}(r_1 - r_2)$$ (3.15)

This immediately leads to the equation for the angular parameter.

$$\phi = \phi_0 + \frac{l}{r_2 - r_1} \tan\theta \sqrt{1 + \left(\frac{r_2 - r_1}{l}\right)^2} \ln\left[r_1 - \frac{z}{l}(r_1 - r_2)\right]$$ (3.16)

By applying the boundary condition $\phi = 0°$ at $z = 0$ mm, ϕ_0 can be obtained as

$$\phi_0 = -\frac{l}{r_2 - r_1} \tan\theta \sqrt{1 + \left(\frac{r_2 - r_1}{l}\right)^2} \ln(r_1)$$ (3.17)

Thus, the mathematic model describing the starting curve of the fiber path can be expressed as

$$\phi = \frac{l}{r_2 - r_1} \tan\theta \sqrt{1 + \left(\frac{r_2 - r_1}{l}\right)^2} \left\{\ln\left[r_1 - \frac{z}{l}(r_1 - r_2)\right] - \ln(r_1)\right\}$$ (3.18)

By substituting Eq.(3.14) and Eq.(3.18) into Eq.(3.1), the equation of the fiber path with a constant helical angle can be written as

$$\begin{cases} x = \left[r_1 - \frac{z}{l}(r_1 - r_2)\right] \cos\left\{\frac{l}{r_2 - r_1} \tan\theta \sqrt{1 + \left(\frac{r_2 - r_1}{l}\right)^2} \left\{\ln\left[r_1 - \frac{z}{l}(r_1 - r_2)\right] - \ln(r_1)\right\}\right\} \\ y = \left[r_1 - \frac{z}{l}(r_1 - r_2)\right] \sin\left\{\frac{l}{r_2 - r_1} \tan\theta \sqrt{1 + \left(\frac{r_2 - r_1}{l}\right)^2} \left\{\ln\left[r_1 - \frac{z}{l}(r_1 - r_2)\right] - \ln(r_1)\right\}\right\} \\ z = z \end{cases}$$ (3.19)

3.2 CATIA Models of Fiber Path Planning

The Visual Basic for Applications (VBA) code was implemented to generate the initial path passing through x-axis, consisting of 1500 points calculated from Eq.(3.19). In the case of multiple sections, the initial curve was circularly patterned about the

revolving axis based upon the number of sections using the circular pattern function built in CATIA. As shown in Figure 3.3, the initial curve and the circularly patterned curves served as both the starting fiber path and the boundary of the sections. The adjacent curve was offset from the reference fiber path along the surface a distance of one tow and ended at either the surface boundary or the initial path. As many parallel paths as needed were placed onto the truncated conical surface in a similar manner until the conical surface was fully covered. Figure 3.4 shows 12 three-dimensional models built for $0°$ and $45°$ plies with six different planning methods. The highlighted regions in the lighter color represent tow dropped areas, where overlapping may occur.
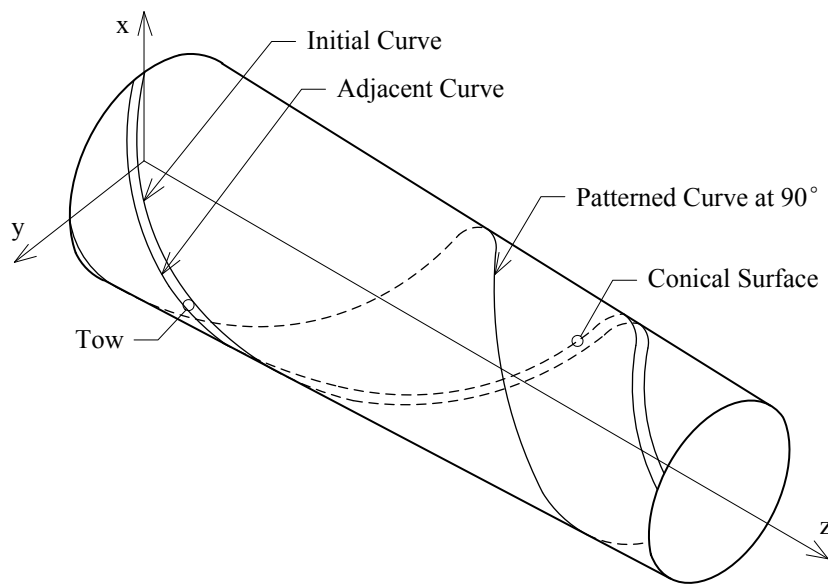
Figure 3.3 Definition of initial curve, patterned curve, and adjacent curve
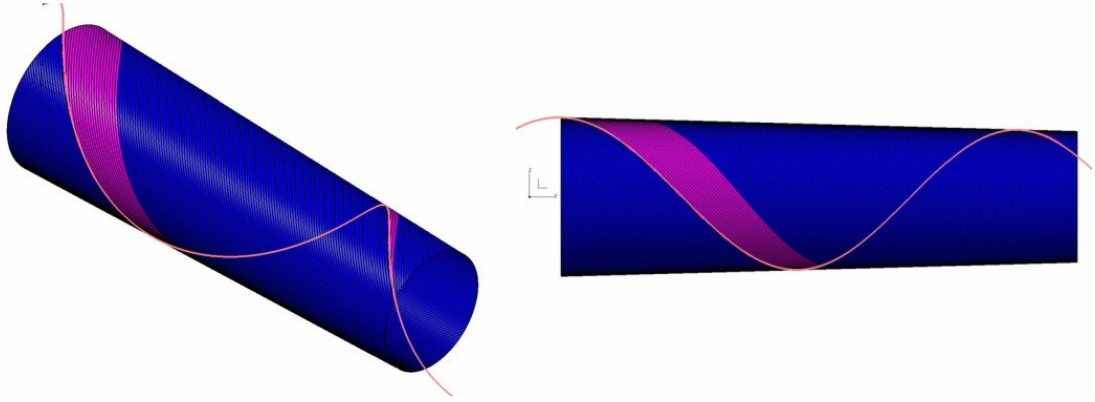
a) Fiber path planning for $45°$ plies with one section
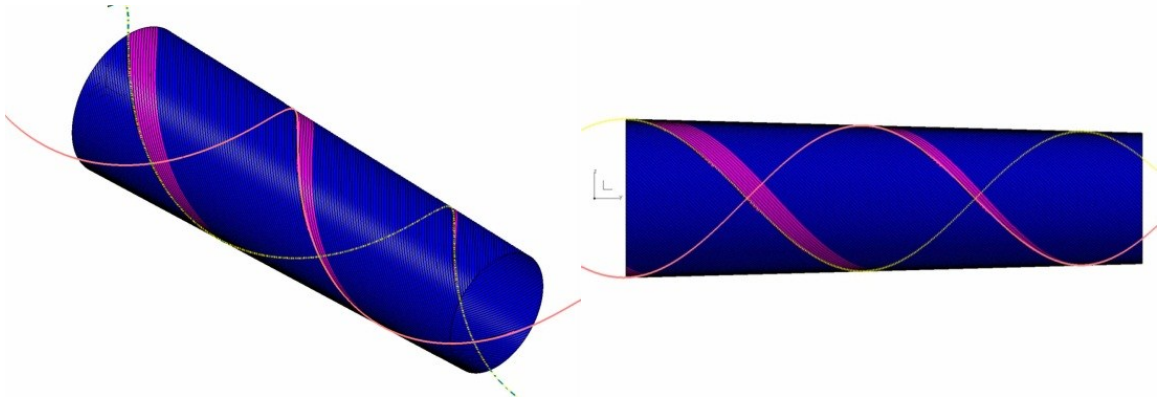
b) Fiber path planning for $45°$ plies with two sections
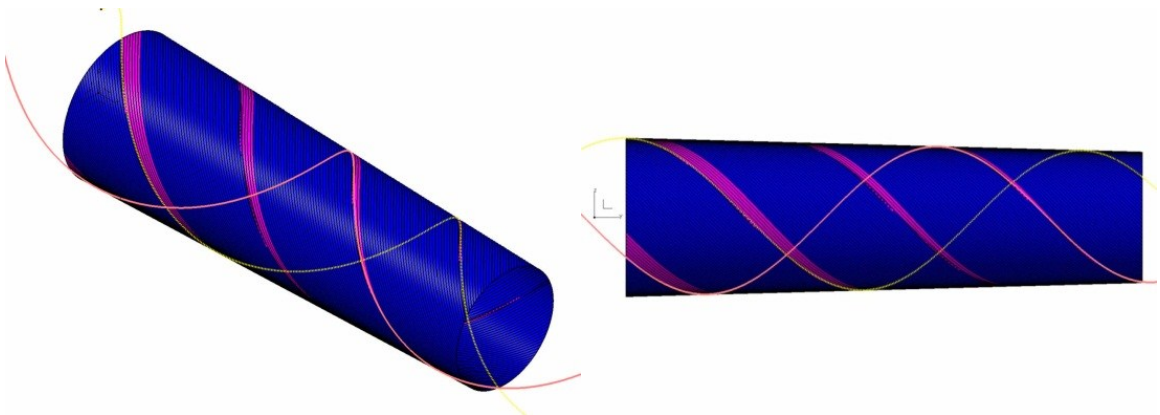
c) Fiber path planning for $45°$ plies with three sections
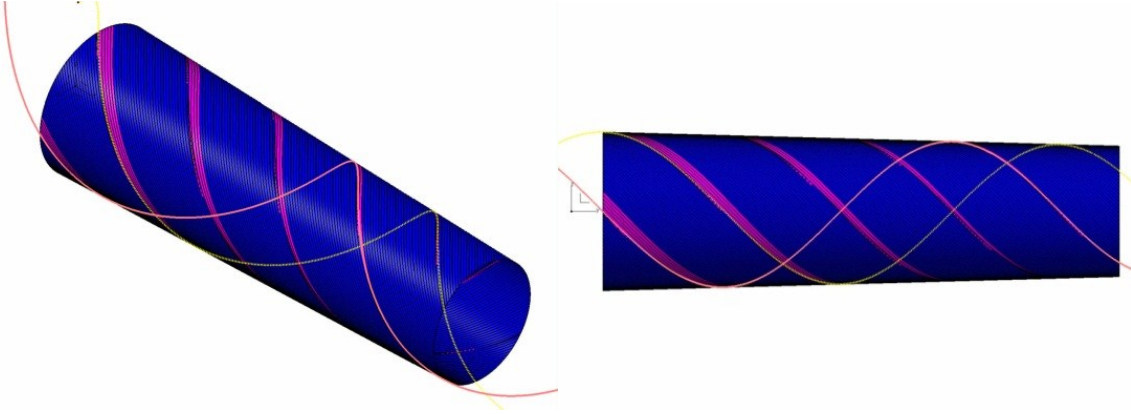
d) Fiber path planning for 45° plies with four sections
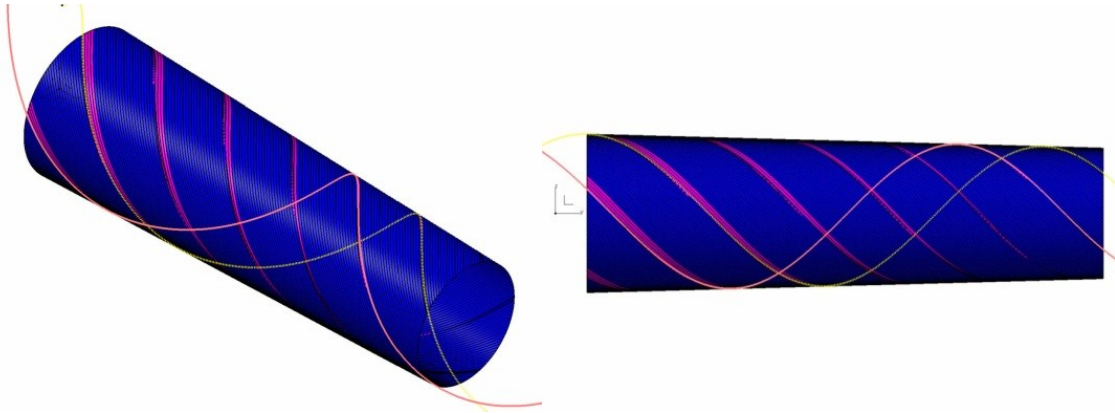
e) Fiber path planning for 45° plies with five sections
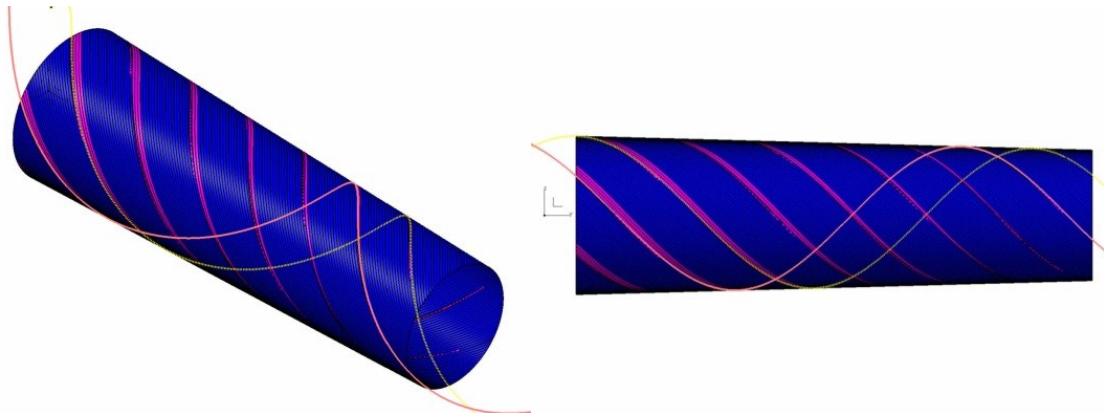
f) Fiber path planning for 45° plies with six sections
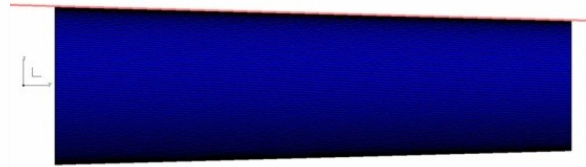
g) Fiber path planning for $0°$ plies with one section

h) Fiber path planning for $0°$ plies with two sections
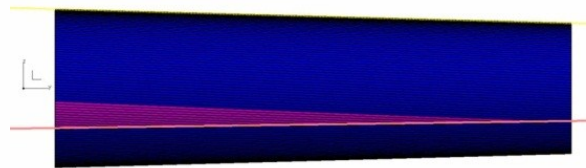
i) Fiber path planning for $0°$ plies with three sections
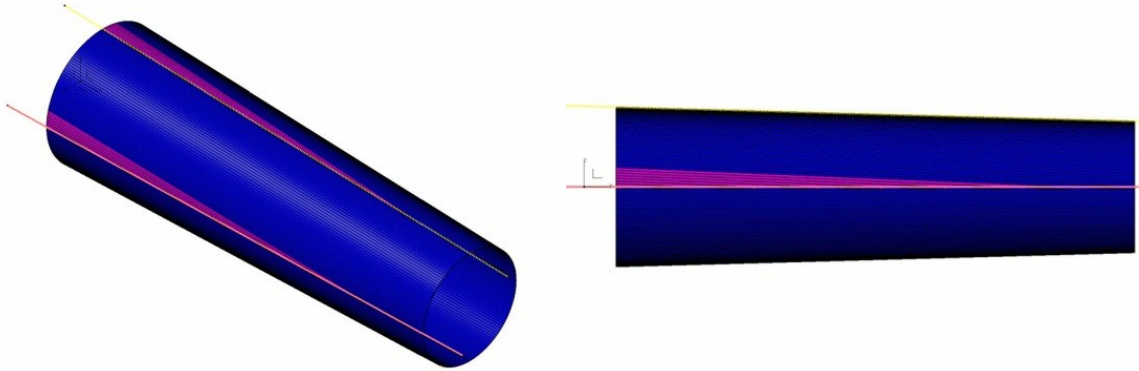
j) Fiber path planning for $0°$ plies with four sections
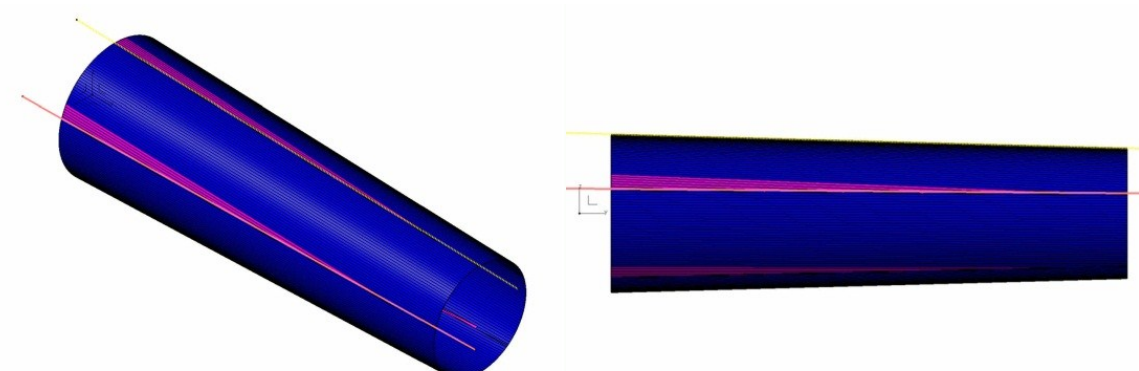
k) Fiber path planning for $0°$ plies with five sections
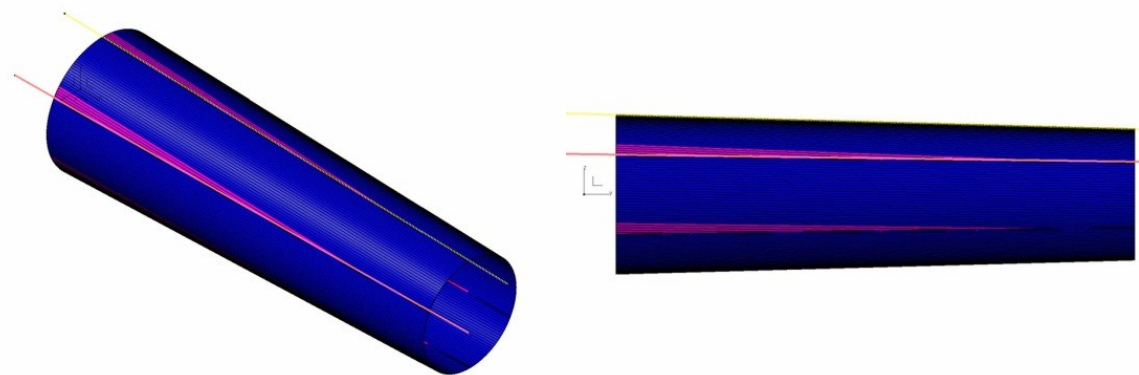
l) Fiber path planning for $0°$ plies with six sections

Figure 3.4 Fiber Path Planning for $0°$ and $45°$ Plies

Upon the completion of the CATIA models, the fiber orientation (θ) at the point-P was measured between the tangent vector of the fiber path and the projected z-axis on the conical surface as shown in Figure 3.5. The angle of deviation was calculated by subtracting the designed fiber orientation from the measured one. The radius of curvature (R) of the curve $a-b$, the intersection of the conical surface and the normal plane to the fiber path, was evaluated by the measuring function in CATIA illustrated in Figure 3.5. The radius of curvature is also known as the minimum compaction roller radius. A CATscript was coded and implemented in CATIA to facilitate the tedious measuring process.
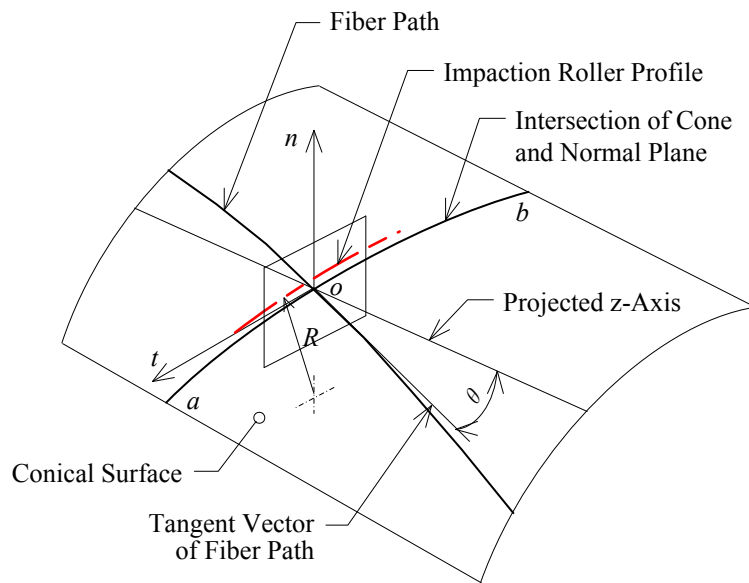
Figure 3.5 Illustration of fiber orientation and radius of curvature

3.3   Analytical Results and Discussion

Figure 3.6 shows the relations between the number of sections and the angle of deviation, and the resulting percentage of laps. While the number of sections increases, the angle of deviation drops exponentially, and the percentage of overlapped area increases linearly. In practice, the initial fiber paths often rotate a constant angle from one

38

ply to another so that the overlapped area would evenly spread out in the laminates. This effectively prevents thickness build-up and minimizes stress concentration. In addition, all 90° plies have a single section, and the tow is placed upon the tool surface at the constant pitch instead of the constant helix angle as used for 0° and ±45° plies.
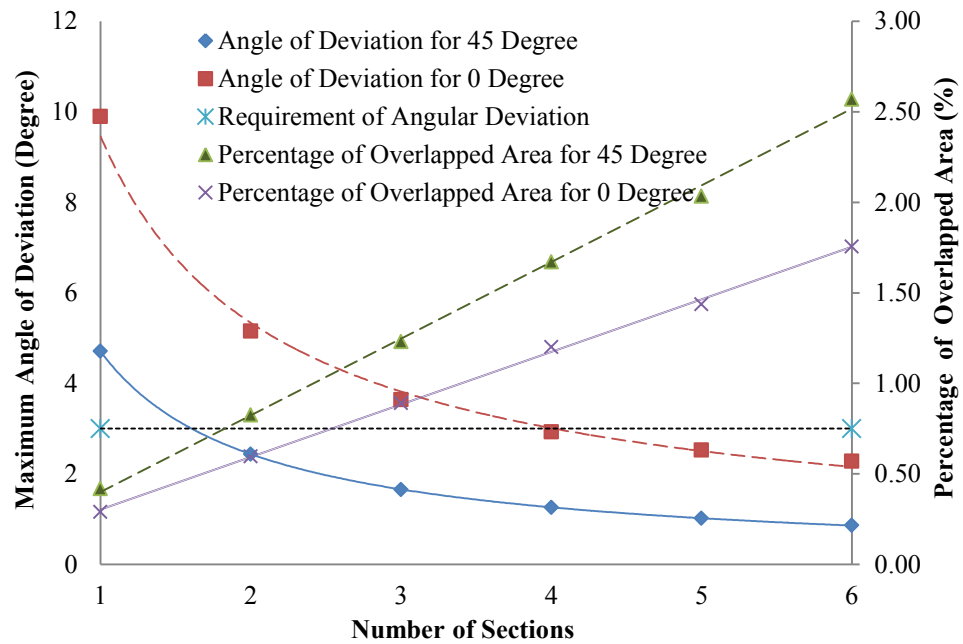
Figure 3.6 Plot of angle of deviation/percentage of overlapped area versus number of sections

CHAPTER 4   Effects of Fiber Placement Induced Defects on Mechanical Behavior of Thermoplastic Composite Laminates

This experimental work investigated the effects of two interlaminar defects, namely gap and overlap, on the strength and stiffness properties of thermoplastic composites at both the lamina level and the laminate level. Five types of mechanical tests were executed in accordance with the ASTM test standards for determining tensile strength and modulus, compression strength and modulus, in-plane shear strength and modulus, open-hole tensile strength and open-hole compression strength. Three sets of specimens for each test were fabricated and tested under the identical testing conditions. Experimental results have been compared with the baseline configuration without the interlaminar defects.

4.1   Description of Interlaminar Defects

While laying down slit tapes on a highly contoured surface such as a truncated conical surface, gaps and laps aligned along the direction of the fiber path are inevitable. It is important for design engineers to understand the combined effects of these defects on the mechanical properties of a fiber placed structural component prior to sizing laminate. Table 4.1 lists the basic mechanical properties of interest and the evaluation methods. However, it is nearly impractical to experimentally examine all combinations of size, location and recurring frequency of defects in any fiber placed laminate. Instead, a systematic study on individual defects with a constant size, location, and recurring frequency could be carried out within the limited time and costs, and still provide a good understanding on the combined cases. Thus, in this experimental work, the defect width is set to 6.35 mm to simulate the worst-case scenario of missing individual tows

encountered during the fiber placement process, and the nominal thickness of the defects is defined as 0.250 mm, twice of single-tow thickness, to capture the variability between different defect configurations. The defects are located along the 0° fiber direction in the mid-plane of a symmetric laminate to minimize the asymmetric effects. Moreover, each specimen contains a single defect for the purpose of simplification.

Table 4.1 Basic mechanical properties and associated ASTM test standards

ASTM Test Method	Measured Property	Coupon Length/Width (mm)	Stacking Sequence
D 3039-07	Tensile Strength and Modulus	254.00/12.70	$[0]_8$
D 3410-03	Compressive Strength and Modulus	139.70/12.70	$[0]_{12}$
D 5379-05	Shear Strength and Modulus	76.20/19.05	$[0/90]_{6S}$
D 6484-04	Open-Hole Tensile Strength	304.80/38.10	$[\pm45/90/0]_{2S}$
D 6484-04	Open-Hole Compressive Strength	304.80/38.10	$[\pm45/90/0]_{4S}$

The defect configurations of gaps and laps are illustrated in Figure 4.1. For example, the gap is made by removing two tows, one on top of each other. While the overlap is created by adding two tows instead of removing them. Figure 4.2 to Figure 4.5 show the specimen configurations of each test with the defect location designated by plane lines in the gage length. In total, nine panels were fabricated for all tests, and the defects were manually inserted during hand layup. The location of each defect was marked on the edge of the laminate with a marker in the trimming area to accurately place the defect in the gage area of the specimen.
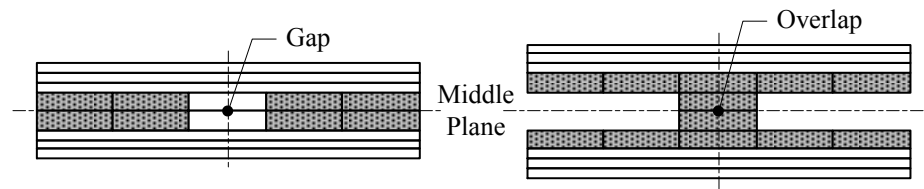
Figure 4.1 Defect configurations of gap (left) and overlap (right)
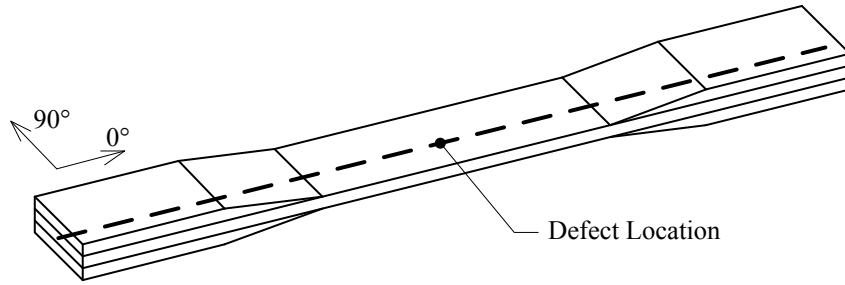
Figure 4.2 Tensile test specimen with interlaminar defect marked on dashed line
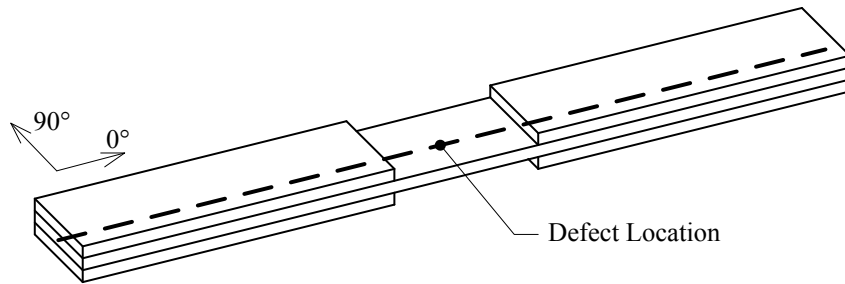
Figure 4.3 Compression test specimen with interlaminar defect marked on dashed line
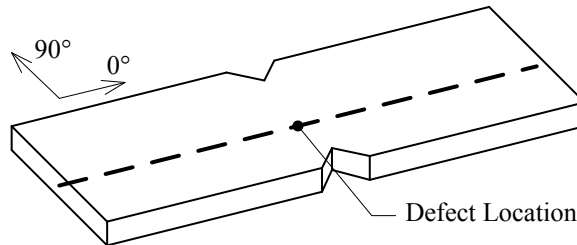
Figure 4.4 V-notched shear test specimen with interlaminar defect marked on dashed line
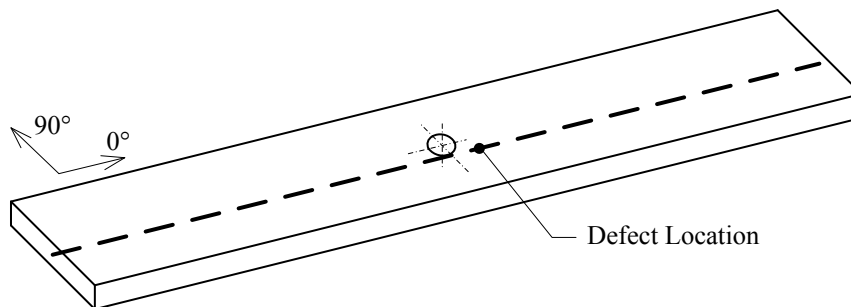
Figure 4.5 Open-hole tensile and compression test specimen with interlaminar defect

marked on dashed line

4.2   Specimen Fabrication

The material used in this study is a 304.8 mm (12 in) wide AS4/PEEK unidirectional tape supplied by Cytec Engineered Materials. The unidirectional tape consists of a 68:32 wt% mixture of AS4 and APC-2 [32]. The typical value of the volume fraction of fibers is 61% [32]. APC-2 is a semi-crystalline high-temperature thermoplastic polymer with a glass transition temperature of 143 °C, a melting point of 342 °C and a recommended processing temperature of 380 - 400 °C [32]. The test panels were molded in a laboratory-size high-temperature autoclave as follows: the laminates were vacuum bagged, evacuated to remove entrapped air, heated in order to melt the matrix material, pressurized from the outside to consolidate the laminate, and finally cooled to solidify the matrix material. Table 4.2 shows the identifications, dimensions, and stacking sequences of all test panels.

Table 4.2 Identifications, dimensions, and stacking sequences of test panels

Panel ID	Number of Panels	Panels Length/Width (mm)	Test Method	Stacking Sequence
PN-1	1	304.80/152.40	D 3039-07	$[0]_8$
PN-2	1	190.50/152.40	D 3410-03	$[0]_{12}$
PN-3	1	127.00/177.80	D 5379-05	$[0/90]_{6S}$
PN-4,5,6	3	355.60/304.80	D 6484-04	$[\pm45/90/0]_{2S}$
PN-7,8,9	3	355.60/304.80	D 6484-04	$[\pm45/90/0]_{4S}$

A cross-section of the vacuum bag assembly for autoclave consolidation of test panels and its use is shown schematically in Figure 4.6, which shows the following: (1) 6.35 mm thick mild steel tool plate supports the entire assembly; (2) 0.744 mm thick stainless steel caul plate ensures the thickness tolerance of autoclave molded panels ; (3) bagging film (Thermalimide, Airtech) coated with release agent (Frekote 770-NC,

Henkel); (4) tack welded laminate; (5) high-temperature sealant tape (SM-5160 Tacky-Tape, Schnee-Morehead); (6) 6 oz. plain woven fiberglass cloth, which prevents the lateral flow of polymers during processing; (7) breather (Airweave UHT 800, Airtech); (8) vacuum valve (Vac Valve 409SSHTR, Airtech.) Additionally, a set of four thermocouples is placed in the middle plane of each test panel for measuring the real-time part temperature and feeding the signal back to the autoclave's control system. As fiber alignment is critical to the resulting laminate properties, prepregs were carefully cut and aligned to within 0.5°, and tack welded in the trim area by a temperature-controlled welding station to prevent movement during assembly. The stacking sequences and dimensions of these test panels are listed in Table 4.2.
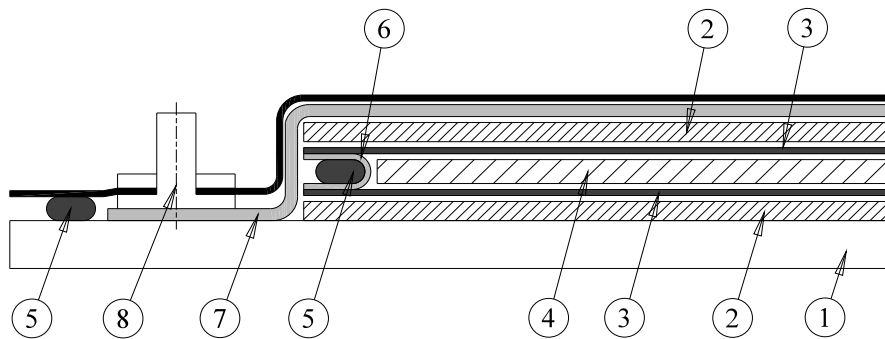
Figure 4.6 Cross-section of vacuum bag assembly for autoclave consolidation

The completed vacuum bagged laminates were then slid into the high-temperature autoclave for consolidation as shown in Figure 4.7. The processing cycle of AS4/APC-2 is illustrated in Figure 4.8. Lystrup and Andersen point out that it is important to pressurize the autoclave throughout the processing cycle to improve heat energy transfer from heating elements by adding more molecules [33].
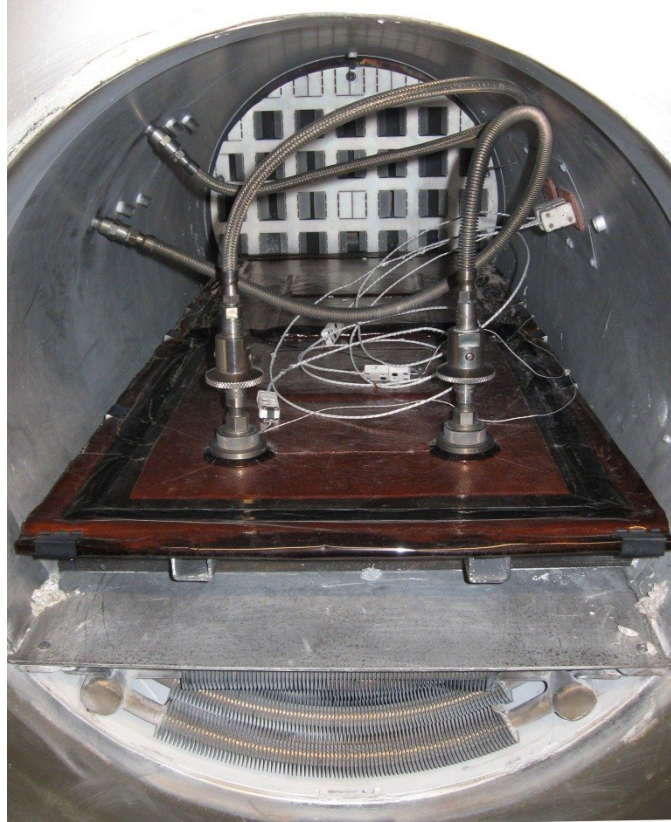
Figure 4.7 Illustration of vacuum bagged laminate in high-temperature autoclave
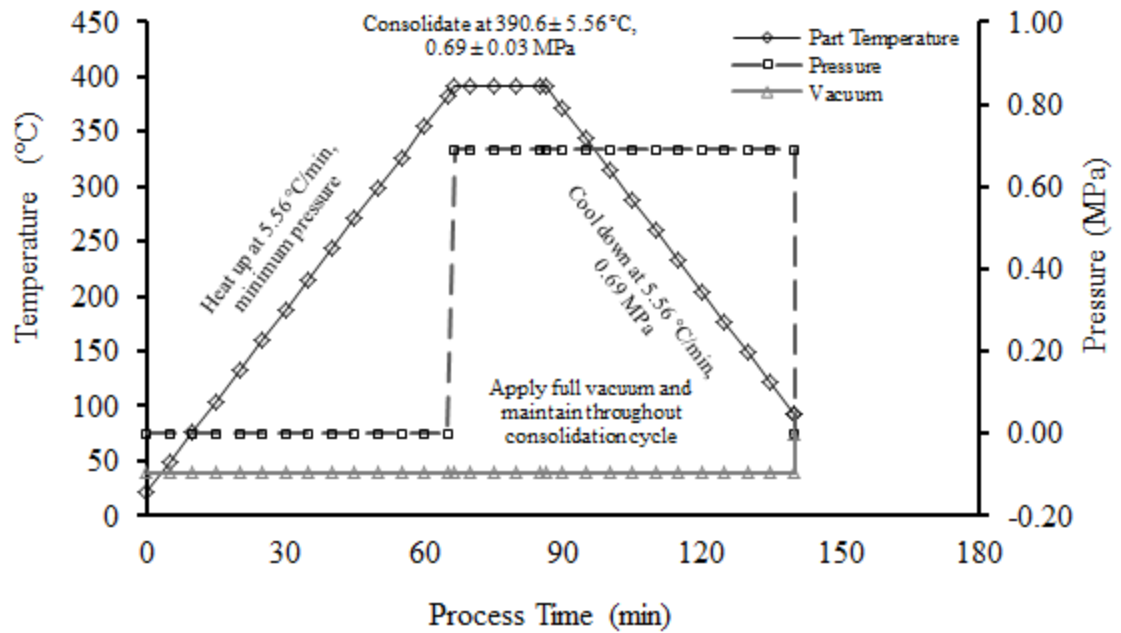
Figure 4.8 Recommended processing cycle of APC-2/AS4 by Cytec

After the vacuum bagged laminates were removed from the autoclave after consolidation, they were cleaned with Frekote® PM-Cleaner™ to remove the remaining release agent from the surface of the molded laminates. Each test coupon was then cut from the test panels using the 6.35 mm diameter polycrystalline diamond (PCD) tipped carbide router (list number: 3867) supplied by GRHRING on a numerically controlled vertical milling machine equipped with a dust collection system. The spindle speed and feed rate were 10,000 RPM and 3,048 mm/min. Hole drilling was performed on the open-hole tensile and compressive test coupons using the router.

4.3   Specimen Test

Both lamina properties, tensile, compression and in-plane shear properties, and laminate properties, open-hole tensile and open-hole compression properties, are evaluated in this work. These properties are essential to understand the behaviour of a real and complex structure under multidirectional loads. All tests, except the open-hole compressive test, were performed on the calibrated MTS hydraulic testing system with a 100 kN load cell with a constant crosshead speed. Five samples were tested for each test so as to obtain a satisfactory average and change variance.

ASTM D 3039-07 was employed to determine tensile strength and modulus. The specimens were instrumented with strain-indication transducers which are centered on the loading axis in the gage section and mounted at 0° to the loading axis [34]. Static loads were introduced progressively into the specimens by hydraulic grips at a standard head displacement rate of 2 mm/min until the load dropped significantly [34]. The tensile moduli were calculated from stress-strain curves within the strain range between 1000 $\mu\varepsilon$ and 3000 $\mu\varepsilon$ [34].

ASTM D 3410-03 was used to evaluate compressive strength and modulus. The specimens were instrumented with back-to-back strain indication transducers which are centered on the loading axis in the gage section and mounted at 0° to the loading axis [35]. An Illinois Institute of Technology Research Institute (IITRI) compression test fixture in accordance with the standard test method was used to provide stability in unnotched compression testing. Static loads were introduced progressively into the specimens via the fixture at a standard head displacement rate of 1.5 mm/min until the load dropped significantly [35]. The compressive moduli were calculated from stress-strain curves within the average strain range between 1000 $\mu\varepsilon$ and 3000 $\mu\varepsilon$ [35].

ASTM D 5379-05 was adopted to examine shear strength and modulus. The specimens were instrumented with strain-indication transducers which were centered on the loading axis in the gage section and mounted at +45° and -45° to the loading axis [36]. The V-notched beam test fixture in conformance with the standard test method was used to provide asymmetric flexure. Static loads were introduced progressively into the specimens via the fixture at a standard head displacement rate of 2 mm/min until the specimens failed [36]. The compressive moduli were calculated from stress-strain curves within the average strain range between 1500 $\mu\varepsilon$ and 2500 $\mu\varepsilon$ [36].

ASTM D 5766-07 was used to determine notched tensile strength. The specimens were mounted parallel to the loading axis. Static loads were introduced progressively into the specimens by hydraulic grips at a standard head displacement rate of 2 mm/min until the load dropped significantly [37]. The open-hole tensile strengths were calculated based on the gross cross-sectional area disregarding hole [37].

ASTM D6484-04 was employed to determine notched compressive strength. The specimens were inserted into a Boeing open-hole compression test fixture which provide lateral support to the test specimens in compression testing, and mounted at 0° to the loading axis [38]. Static loads were introduced progressively into the specimens via the fixture at a standard head displacement rate of 2 mm/min until the load dropped significantly [38]. The open-hole compressive strengths were calculated based on the gross cross-sectional area disregarding the hole.

4.4   Experimental Results

Those specimens without the interlaminar defects are labeled as baseline specimens. Each test value represents the average of five samples. Table 4.3 presents the experimental results obtained from the tensile tests. The failure mode is identified as longitudinal splitting located in the middle of gage area for all tests. The experimental results imply that the influence of the interlaminar defects on the tensile properties is minimal. The tensile strength and modulus for the gap configuration decreases from the baseline by 5.07 % and 1.89 % respectively. The mechanical properties for the overlap configuration are negligibly changed. The maximum observed 2.66 % sample coefficient of variation suggests consistent and representative results for all test configurations.

Table 4.3 Summary of tensile modulus and strength of test coupons without and with

interlaminar defects

Defect Type	Tensile Modulus (GPa)			Tensile Strength (MPa)		
	Average Value	Standard Deviation	Coeff. of Variation	Average Value	Standard Deviation	Coeff. of Variation
Basline	135.73	3.61	2.66	2446.22	44.34	1.81
Gap	133.17	0.47	0.35	2322.20	33.95	1.46
Overlap	136.37	1.46	1.07	2467.42	30.02	1.22

Table 4.4 tabulates the experimental results obtained from the compression tests. The failure mode is identified as brooming located in the middle of gage area for all tests. The experimental results show that the influence of the interlaminar defects on the compressive properties is negligible. The compressive strength and modulus for the gap configuration decreases by 5.27 % and 1.21 % respectively. The compressive strength for the overlap configuration increases by 1.76 %. The maximum observed 0.83 % sample coefficient of variation suggests consistent and representative results for all test configurations.

Table 4.4 Summary of compressive modulus and strength of test coupons without and

with interlaminar defects

Interlaminar Defect	Compressive Modulus (GPa)			Compressive Strength (MPa)		
	Average Value	Standard Deviation	Coeff. of Variation	Average Value	Standard Deviation	Coeff. of Variation
Basline	123.10	0.40	0.32	1406.61	9.44	0.67
Gap	122.90	0.40	0.33	1332.52	11.09	0.83
Overlap	123.90	0.70	0.56	1431.35	10.63	0.74

Table 4.5 lists the experimental results obtained from the in-plane shear tests. The experimental results show that the influence of the interlaminar defects on the compressive properties is negligible. The shear strength and modulus for the gap configuration decreases from the baseline by 1.17 % and 1.82 % respectively. The compressive strength for the overlap configuration increases by 2.57 %. The 3.64 % sample coefficient of variation suggests consistent and representative results for all test configurations.

Table 4.5 Summary of in-plane shear modulus and strength of test coupons without and with interlaminar defects

Interlaminar Defect	In-Plane Shear Modulus (GPa)			In-Plane Shear Strength (MPa)		
	Average Value	Standard Deviation	Coeff. of Variation	Average Value	Standard Deviation	Coeff. of Variation
Basline	5.50	0.20	3.64	80.09	1.27	1.59
Gap	5.40	0.10	1.85	79.15	1.96	2.48
Overlap	5.50	0.20	3.64	78.03	1.54	1.97

Table 4.6 shows the experimental results obtained from the open-hole tensile tests. The specimens fail in tension at the hole, but remnants of angle plies cross the hole lateral centerline. The experimental results show that the influence of the interlaminar defects on the notched tensile properties is minimal. The open-hole tensile strength decreases from the baseline by 5.14 % for the gap configuration and 2.93 % for the overlap configuration. The 1.57 % sample coefficient of variation suggests consistent and representative results for all test configurations.

Table 4.6 Summary of open-hole tensile strength of test coupons without and with

interlaminar defects

Interlaminar Defect	Open-Hole Tensile Strength (MPa)		
	Average Value	Standard Deviation	Coeff. of Variation
Basline	420.53	4.19	1.00
Gap	398.90	6.25	1.57
Overlap	408.21	5.59	1.37

Table 4.7 presents the experimental results obtained from open-hole compression tests. The specimens fail in compression at the hole and exhibit multiple modes of failure in various sublaminates. The experimental results show that the influence of the interlaminar defects on the compressive properties is negligible. The open-hole compression strength increases over the baseline by 1.23% for the gap configuration and 2.57 % for the overlap configuration. The 2.55 % sample coefficient of variation suggests consistent and representative results for all test configurations.

Table 4.7 Summary of open-hole compression strength of test coupons without and with

interlaminar defects

Interlaminar Defect	Open-Hole Compressive Strength (MPa)		
	Average Value	Standard Deviation	Coeff. of Variation
Basline	335.88	8.56	2.55
Gap	340.00	5.71	1.68
Overlap	344.50	6.34	1.84

4.5   Micrograph Analysis

Figure 4.9 shows a photomicrograph of the polished cross-section of an open-hole compression specimen without interlaminar defects using the optical microscope (Olympus GX71) viewed at the magnification of 5X. Figure 4.10 and Figure 4.11 show the polished cross-section of the open-hole compression specimen with interlaminar defects. It can be observed that overlaps and gaps cause out-of-plane waviness in adjacent plies. The distortion in the laminates is perfectly symmetric about the mid-planes. The materials in the adjacent plies have the ability to move laterally to compensate for local thickness variation. It can be concluded that laminates thickness is not a function of the interlaminar defects for any autoclave molded laminate.

Figure 4.9 Photomicrograph of polished cross-section of open-hole compression specimen without interlaminar defects
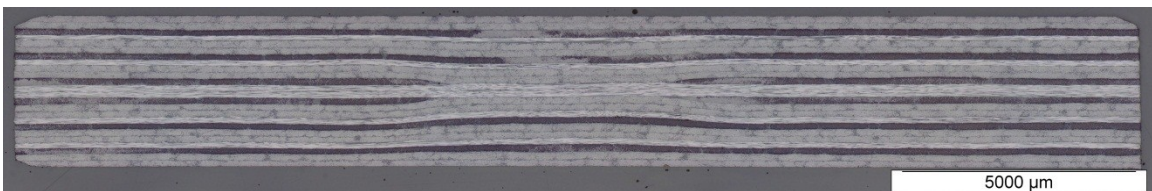
Figure 4.10 Photomicrograph of polished cross-section of open-hole compression specimen with a 6.35 mm wide gap
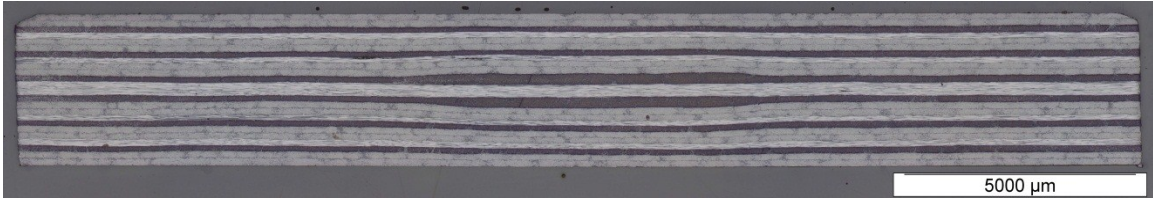
Figure 4.11 Photomicrograph of polished cross-section of open-hole compression specimen with a 6.35 mm wide overlap

4.6   Discussion

The experimental investigation suggests that interlaminar defects have a minimal effect on the mechanical performance of an autoclave molded thermoplastic composite laminate. The photomicrographs show that the defects cause the out-of-plane waviness on the adjacent plies, which may affect the mechanical properties in the 90 ° fiber directions. However, it would be expected that the interlaminar defects have severe effects on the mechanical behaviour of fiber placed laminates fabricated without the autoclave molding process. The material movement described in the previous section is limited to the contact point of incoming material and substrate, which might not be effective for filling up the gaps or evening out the overlaps. Thus, it is more critical for researchers to understand the influence of gaps and overlaps on the mechanical behaviour of a fiber placed laminate and compare with that of an autoclave molded laminate. Although a tremendous effort has been put into the research to fabricate flat test panels as shown in Figure 4.12, the resulting laminate quality is not satisfactory due to the presence of unexpected warpage. Figure 4.13 demonstrates that the test panel is warped after removing it from a heated work table. It still requires more efforts from researchers to provide feasible solutions in the manufacturing of open surface thermoplastic composite panels with good dimension stability.

53
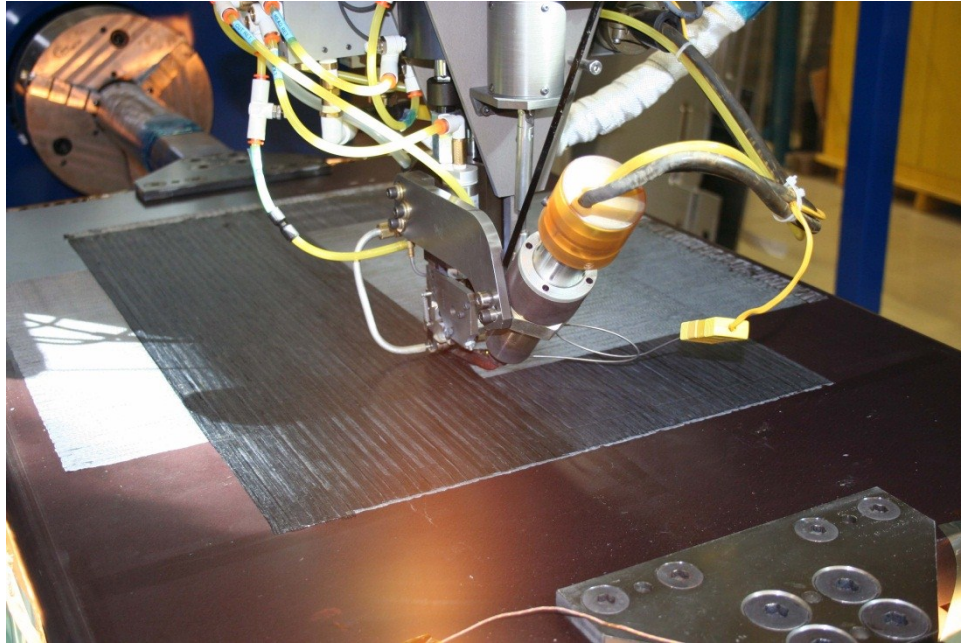
Figure 4.12 Illustration of manufacturing flat test panel using AFP (photo courtesy of the

National Research Council Canada)

Figure 4.13 Illustration of warped fiber placed unidirectional laminate

CHAPTER 5   Development of Optimum Process Condition for Processing AS4/APC-2 Thermoplastic Composites by Automated Fiber Placement

This study focuses on finding the optimum process condition for manufacturing AS4/APC-2 composite rings on a fiber placement system based on interlaminar shear strength. Moreover, the acquired knowledge and experiences from this experimental work on how to fabricate a sound fiber placed composite structure are highly valuable for manufacturing demonstration articles on the same fiber placement work cell. The Taguchi method was adopted in the design of experiments and the statistical analysis of experimental results. Nine composite rings were fabricated on a fiber placement work cell at AMTC with pre-designed processing parameters, and then tested on a hydraulic testing system in accordance with ASTM standard D2344M-00 to determine the interlaminar shear strength and shear strain. The optimum condition was extrapolated based on the experimental results from this study with the use of the Qualiteck-4.

5.1   Design of Experiment - Taguchi's Method

Four principle process variables, namely nozzle temperature, nozzle location, process rate, and compaction force, were selected as major influencing factors for the design of experiment by the experts. Figure 5.1 illustrates that the nozzle temperature is the real-time measurement taken at the center of the outlet of the nozzle by a shielded thermocouple; the nozzle location is the horizontal distance between the nip point of the compaction roller and the outmost point of the torch nozzle; the process rate is the moving speed of the thermoplastic fiber placement head relative to the substrate; and the compaction force is the pressure exerted on the incoming tape by means of the

compaction roller. Although the nitrogen flow influences the resulting laminate quality as reported in the open literature, the nitrogen flow rate in this study was intentionally set to a constant rate of 70 SLPM recommended by ADC to extend the lifetime of a hot gas torch (HGT.) Other uncontrollable processing parameters such as substrate temperature and compaction roller temperature were excluded from the study for the sake of simplification.
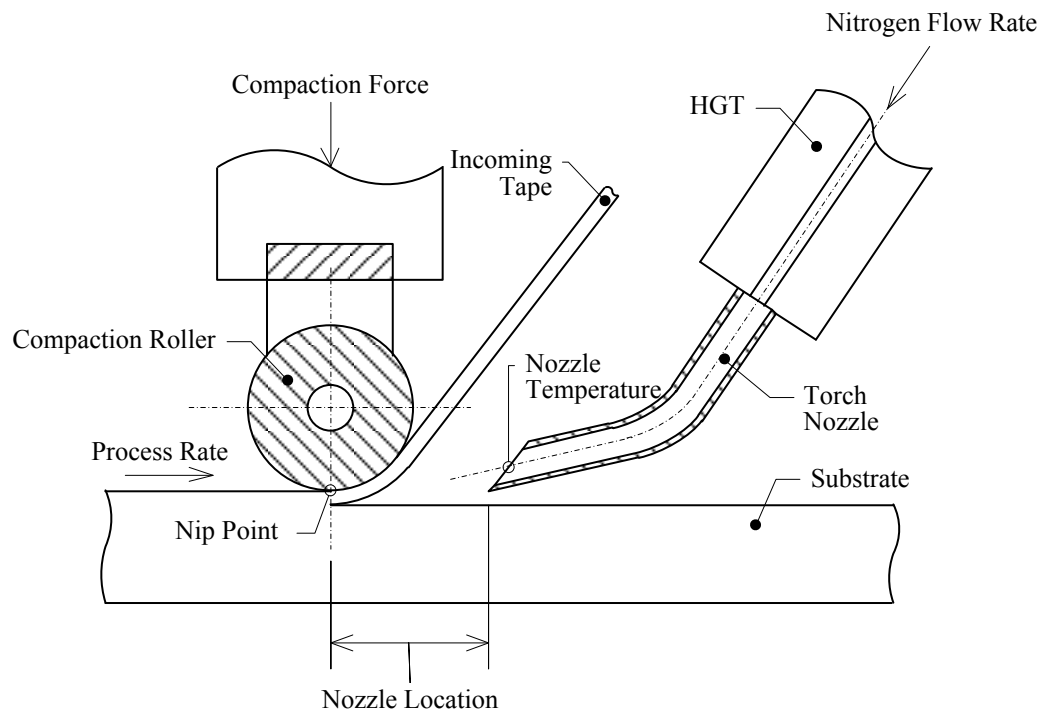
Figure 5.1 Illustration of processing parameters of fiber placement process

Each parameter was assigned three levels to reflect the nonlinearity of factor influences as shown in Table 5.1. If all possible combinations were to be tested, the number of tests would be 81 trials which are impractical in terms of time and cost. In contrast, the use of the Taguchi's method effectively reduces the number of trials and provides insight into the interaction between the variables [39]. The method is developed based on the concept of the orthogonal array which has been widely implemented in

designing experiments. The experiments are laid out using a L-9 array consisting of four factors with three levels as shown in Table 5.2. The first factor was assigned to the nozzle temperature, the second to the process rate, the third to the compaction force, and the fourth to the torch location. The response of the study was identified as the interlaminar shear strength of the fiber placed thermoplastic rings. The influence of each factor and interaction is assessed by the average effects and the analysis of variance (ANOVA). The Qualiteck-4 by Nutek is adopted for analyzing the data from the experiments.

Table 5.1 Description of influencing factors and their levels

Factors	Level 1	Level 2	Level 3
Nozzle Temperature (°C)	900	925	950
Process Rate (mm/sec)	25.4	50.8	76.2
Compaction Force (kgf)	30	40	50
Nozzle Location (mm)	11.38	17.77	21.62

Table 5.2 L-9 Orthogonal array with level descriptions

Trial	Nozzle Temperature (°C)	Process Rate (mm/sec)	Compaction Force (kgf)	Nozzle Location (mm)
1	900	25.4	30	11.38
2	900	50.8	40	17.77
3	900	76.2	50	21.62
4	925	25.4	40	21.62
5	925	50.8	50	11.38
6	925	76.2	30	17.77
7	950	25.4	50	17.77
8	950	50.8	30	21.62
9	950	76.2	40	11.38

5.2   Specimen Fabrication and Inspection

The selected material is AS4/APC-2 unidirectional slit tape from Cytec. The nominal width and thickness of the slit tape are 12.446 mm (0.5 in) and 0.125 mm (0.005 in). The slit tape consists of a 68:32 wt% mixture of carbon fiber (AS4) and PEEK

(APC-2) [32]. The melting temperature (T_m) determined by the Differential Scanning Calorimetry (DSC) analysis is at 346.1°C. The designed layup sequence is $[0]_{50}$, which meets the requirements of the specimen configurations specified in the standard test method for short-beam strength of polymer matrix composite materials and their laminates [40]. Nine thermoplastic composite rings were fabricated individually using the fiber placement system equipped with the thermoplastic fiber placing head shown in Figure 5.2. The slit tape was directly laid onto an unheated cylindrical aluminum mandrel with the diameter of 146.05 mm (5.75 in).
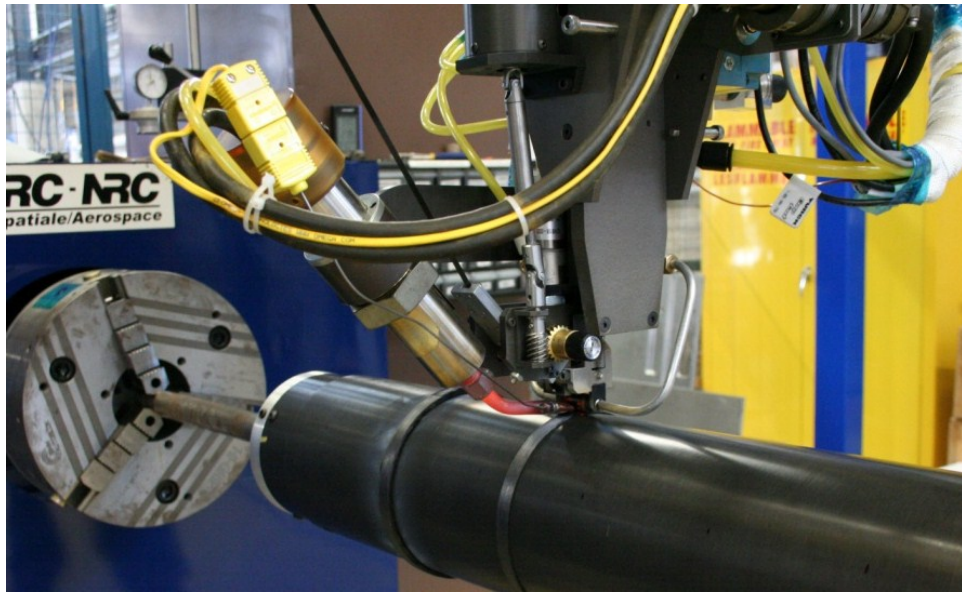
Figure 5.2 6-axis gantry-type fiber placement system equipped with the thermoplastic

fiber placing head (photo courtesy of the National Research Council Canada)

After the fiber placement process, the composite rings were slid off from the contracted aluminum mandrel which was filled up with dry ice. The two end surfaces of the rings were then cleaned by a digital-controlled lathe to facilitate the measurements by the Mitutoyo coordinate-measuring machine (CMM) located at the Engineering Design and Manufacturing Laboratory of Concordia University. The average inner diameter of

the rings was evaluated based on eight measuring points which are evenly distributed on the circumference of the inner circle. The measurements show that the dimensional stability of the fiber placed rings is excellent. Specifically, the variation of the measured inner diameters is within 0.16 mm, and the in-plane deformation of the rings is unnoticeable. It should be pointed out that the thermal expansion of the aluminum mandrel causes an increase in the inner diameter. For instance, the actual diameter of the mandrel measured at the end of the specimen fabrication increased by 0.22 mm. As the nominal ply thickness of the slit tape is 0.125 mm, the ring thickness is expected to be 6.25 mm. However, the measurements show that the thickness of the rings could be reduced by up to 48.18 % by varying the process parameters. Figure 5.3 shows the interrelations of the ring width and the ring thickness in the form of second-order polynomial.

Table 5.3 Average inner diameter and deviation of fiber placed composite rings

Trial	Average Inner Diameter (mm)	Diameter Deviation (mm)	Ring Thickness (mm)	Average Ply Thickness (mm)	Average Tow Width (mm)
1	146.190	0.02616	4.691	0.092	10.56
2	146.129	0.01626	4.633	0.101	9.88
3	146.223	0.02362	5.636	0.119	8.58
4	146.230	0.01702	3.952	0.080	11.86
5	146.106	0.01467	4.039	0.090	11.55
6	146.195	0.01245	5.296	0.109	9.14
7	146.228	0.01651	3.239	0.070	15.07
8	146.266	0.01143	5.024	0.099	9.49
9	146.162	0.01549	4.394	0.090	10.19

The composite rings were then split into halves with a diamond plated saw and measured using the CMM to determine the in-plane deformation induced by the residual stresses. Table 5.4 lists the measured inner diameter of the rings and its deviation after

the splitting. The diametrical deviation indicates that the remaining halves have a favorable circularity similar to the full rings. The reduction of the inner diameter suggests the presence of residual stresses considered in the rings as a byproduct of the fiber placement process. Figure 5.4 shows the in-plane deformations of Trial 3 and Trial 5 which are similar to that of filament wound rings reported by Cirino and Pipes [41]. They demonstrated that the state of stress in the wound rings changes due to the mechanical and thermal loads experienced during the winding process [41]. Winding tension is effective in controlling the state of stress induced in the ring during the winding process. Appling a constant or linearly increasing tension with each ply resulted in a compressive radial stress distributed in the ring [41]. Applying a winding tension that linearly decreased with each ply, however, resulted in a tensile radial stress distribution in the ring. It is reported that the in-situ consolidation process reduces the magnitude of the residual stress in the ring relative to those resulting from the post consolidation process [41].

$$y = 2244.4x^2 - 547.86x + 42.109$$
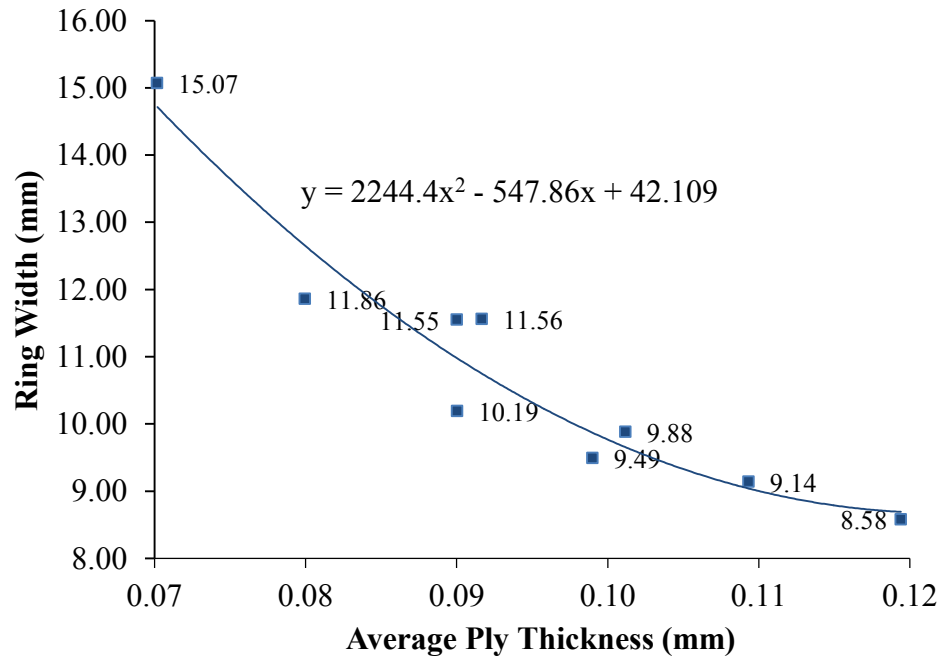
Figure 5.3 Plot of ring width versus ply thickness

Table 5.4 Inner diameter of composite rings after splitting

| Trial | Inner Diameter (mm) | | | | Percent |
	Before Splitting	Deviation	After Splitting	Deviation	Change
1	146.190	0.0262	143.916	0.0218	-1.56
2	146.129	0.0163	145.059	0.0061	-0.73
3	146.223	0.0236	146.413	0.0107	0.13
4	146.230	0.0170	144.663	0.0122	-1.07
5	146.106	0.0147	143.680	0.0112	-1.66
6	146.195	0.0124	145.385	0.0102	-0.55
7	146.228	0.0165	144.211	0.0112	-1.38
8	146.266	0.0114	144.823	0.0099	-0.99
9	146.162	0.0155	144.140	0.0132	-1.38
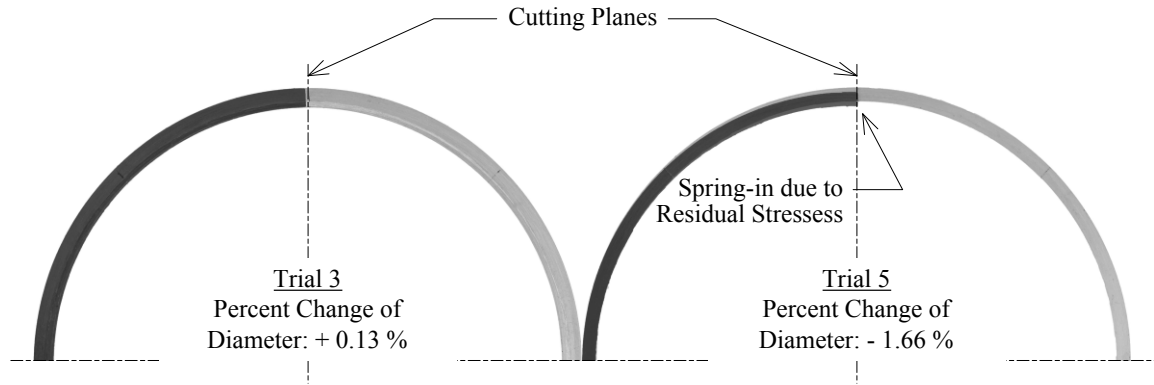
Figure 5.4 Comparison of Trial 3 (left) and Trial 5 (right) before splitting (colored in grey) and after splitting (colored in black)

Lastly, curved specimens were machined off from the opened rings by the 6.35 mm diameter PCD tipped carbide router (list number: 3867) supplied by GRHRING on a numerically controlled vertical milling machine equipped with a dust collection system located at Precimax so that the requirements of geometrical tolerance and surface roughness illustrated in Figure 5.5 would be completely satisfied. Prior to testing, specimens were moisture conditioned by continuous exposure to $23 \pm 3\,°C$ and $50 \pm 10\,\%$ relative humidity for 72 hours.
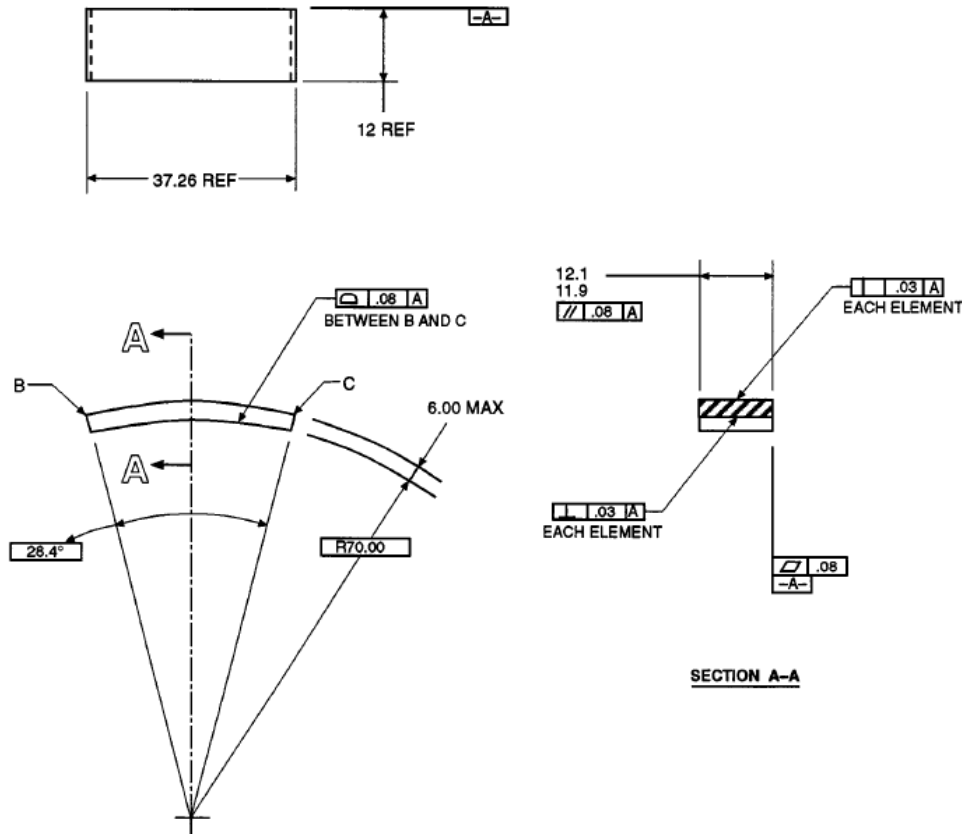
Figure 5.5 Curved specimen configurations [40]

5.3   Short Beam Strength and Interlaminar Shear Strain

Short beam shear tests were carried out according to the ASTM standard D2344M-00. The test fixture purchased from the Wyoming Test Fixtures was used to align and center specimens so that its longitudinal axis would be perpendicular to the loading nose and side supports. The loading nose was located equidistant between the side supports within ± 0.03 mm. Both the loading nose and the side support overhung the specimen width by at least ± 2 mm at each side. The tests were performed on a MTS hydraulic testing system at room temperature with a 100 kN load cell with a crosshead speed of 1 mm/min. The specimens were mechanically tested to a load drop-off of 30 %. Five samples were tested for each ring so as to obtain a satisfactory average and standard

deviation. The first maximum load was recorded as the failure load. The short-beam strength (or interlaminar shear strength) is calculated as follows:

$$F^{sbs} = 0.75 \times \frac{P_m}{b \times h} \tag{5.1}$$

where P_m is the first maximum load observed during the test, b is the measured specimen width, h is the measured specimen thickness.

Interlaminar shear strains were measured by the Vic-3D digital image correlation system by Correlated Solutions equipped with two 28 mm digital lenses. Figure 5.6 shows the test setup for three-dimensional correlation measurements on a curved short-beam test specimen. The speckle pattern was applied by first coating the specimens with a layer of black paint using a spray can. The white speckles were then applied by lightly over-spraying a white mist of paint. A series of speckle images were acquired along the course of the short-beam shear tests. The maximum interlaminar shear strain at the failure load was recorded. The strain measurements were performed by Farjad Shadmehri with assistance of the author at the laboratory of CONCOM.

Figure 5.6 Test setup for 3D image correlation measurements

5.4   Experimental Results

A summary of the short-beam strengths and the interlaminar shear strains is presented in Table 5.5. Subsequent strength comparisons that evaluate the average effects of process parameters are based upon the tabulated experimental results. The short-beam strength varies from 31.3 MPa to 47.5 MPa with changing process parameters. Among nine trials, the fourth trial (925 ºC nozzle temperature, 25.4 mm/sec process rate, 40 kgf compaction force, and 21.62 mm nozzle location) delivers the best mechanical performance, and the third one exhibits the lowest short-beam strength. Low standard deviation implies that the experimental results are consistent and representative for all specimens.

A typical distribution of interlaminar shear strain of the short-beam specimen prior to the ultimate failure is shown in Figure 5.7. It is observed that the shear strain distribution on the right-hand side of the mid- plane has a positive shear strain and the

one on the left-hand side of the mid-plane has a negative shear strain. The shear strain distribution is nearly symmetric to the mid-plane, and the stress concentration due to the local deformation at the load point is observed. This implies that the specimen is properly aligned with the loading direction so that the measured interlaminate shear strength would be representative of the entire population.
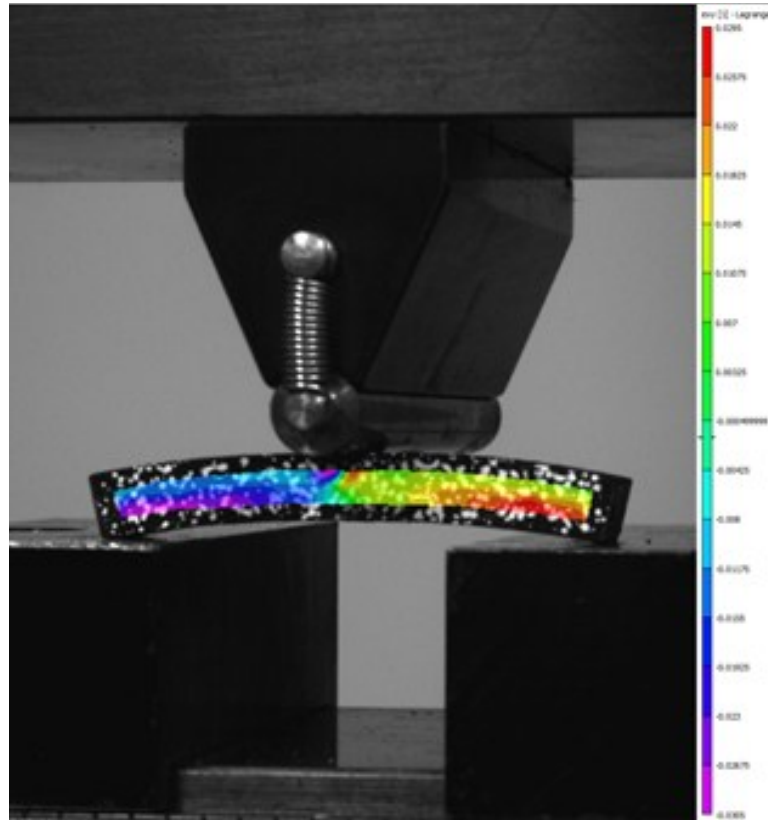
Figure 5.7 Through-thickness shear strain field acquired by Vic-3D system

Table 5.5 Experimental results of short-beam strength and interlaminar shear strain

Trial	Short-beam Strength (MPa)		Interlaminar Shear Strain	
	Average	Std. Dev.	Average	Std. Dev.
1	43.9	4.3	1.100	0.071
2	45.0	0.7	0.957	0.009
3	31.3	1.0	0.597	0.068
4	47.5	1.6	1.227	0.083
5	42.8	1.8	0.723	0.017
6	39.9	1.0	1.300	0.143
7	34.8	1.8	1.223	0.113
8	41.4	1.0	1.172	0.155
9	41.9	2.0	0.990	0.016

Figure 5.9a-i illustrate the failure mode of the tested specimens under the microscope which was identified as intralaminar shear as opposed to interlaminar shear. The polished cross-section was located at the end of the specimen where cracks initiated and propagated. The photomicrographs show that cracks initiate and propagate within the plies, and jump through the bonding interface of adjacent plies. It can be concluded that the fiber placed laminate quality strongly depends on the intralaminar shear strength.
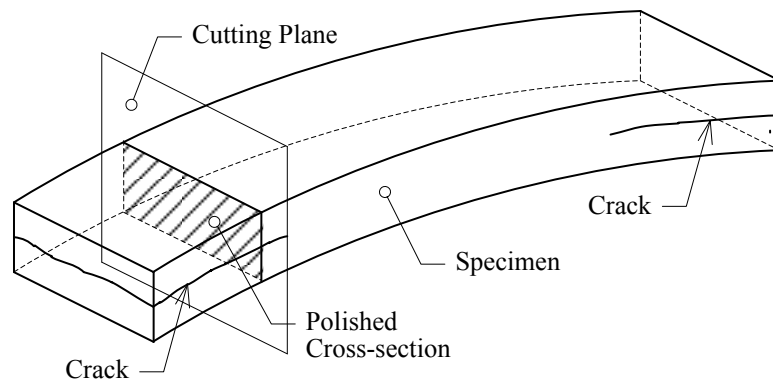
Figure 5.8 Location of polished cross-section of specimen

a) Trial 1
    Failure Mode: Intralaminar Shear

200 µm

b) Trial 2
    Failure Mode: Intralaminar Shear

200 µm
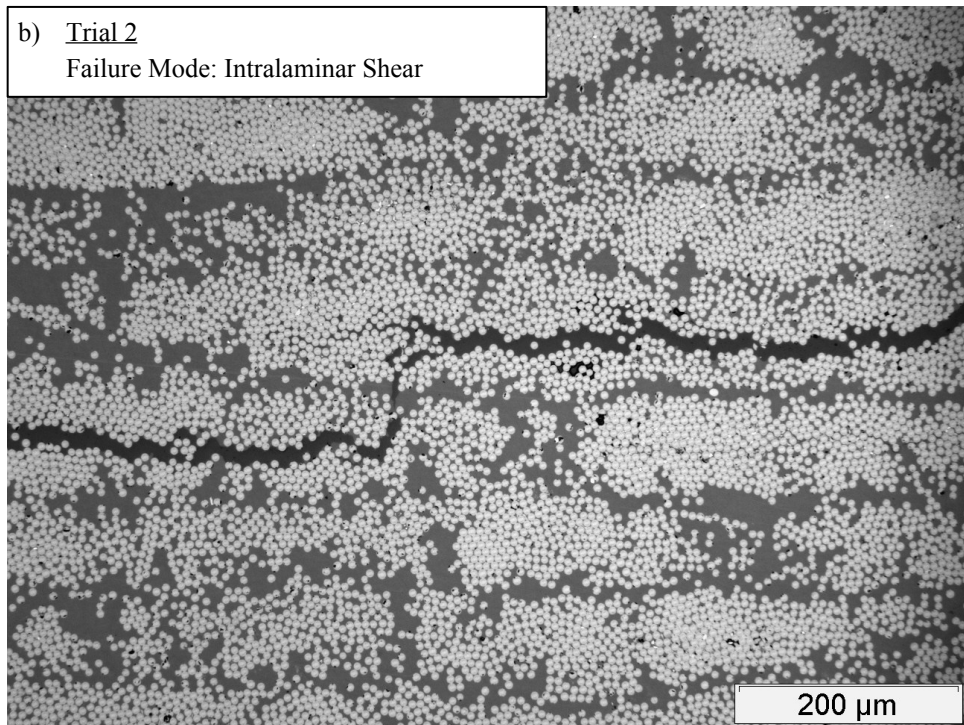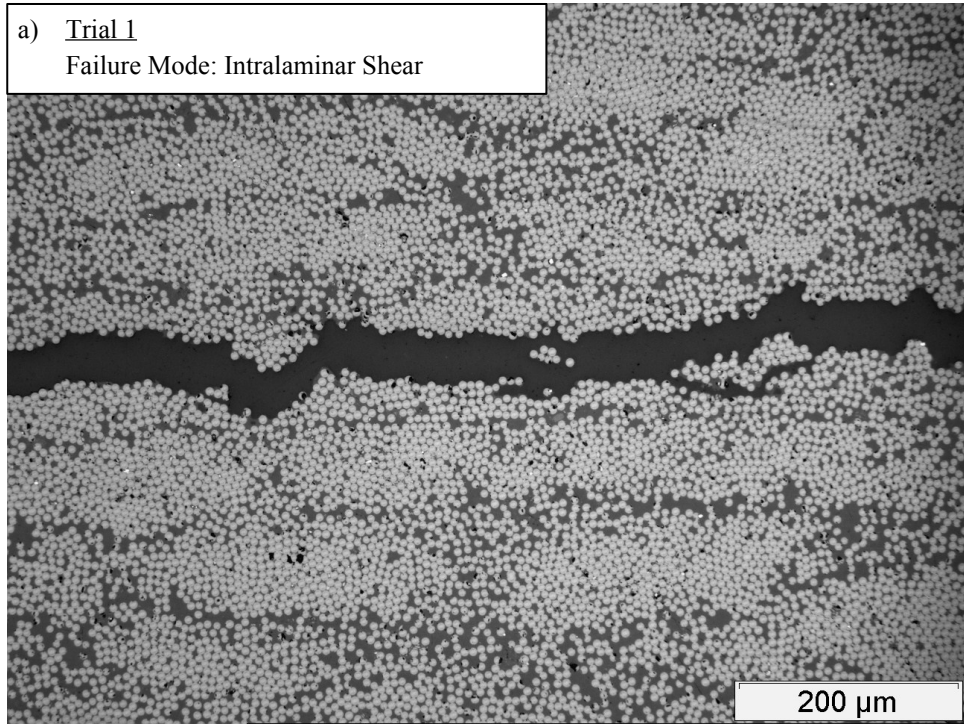
c) Trial 3
Failure Mode: Intralaminar Shear

200 µm
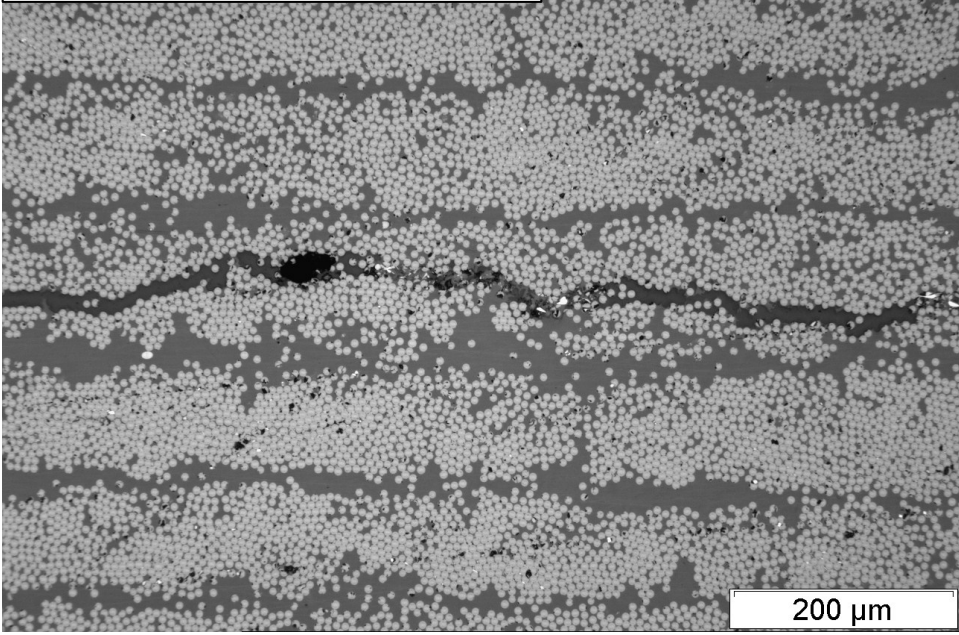
d) Trial 4
Failure Mode: Intralaminar Shear

200 µm
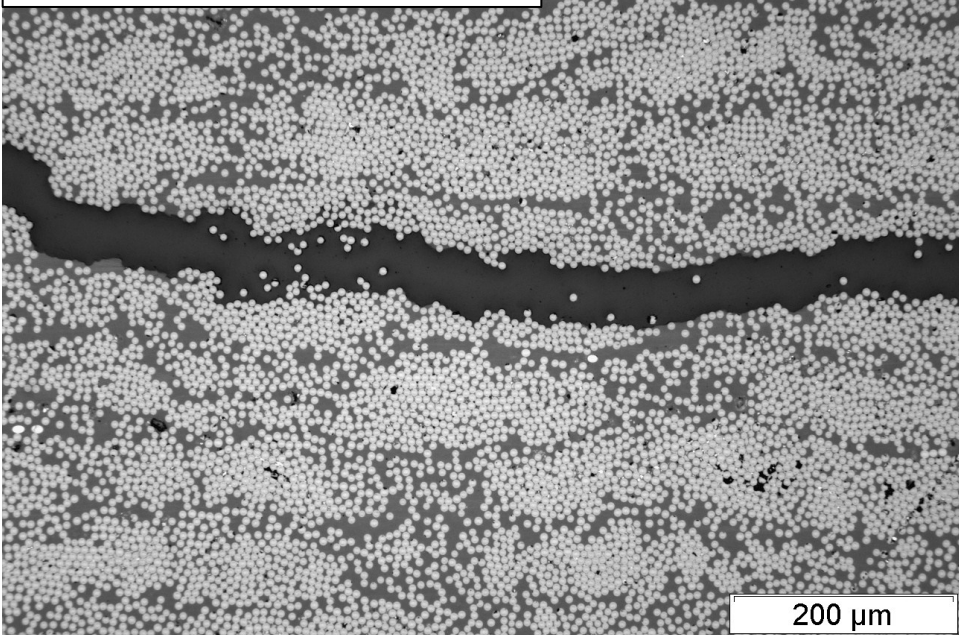
e)   Trial 5
      Failure Mode: Intralaminar Shear

200 µm
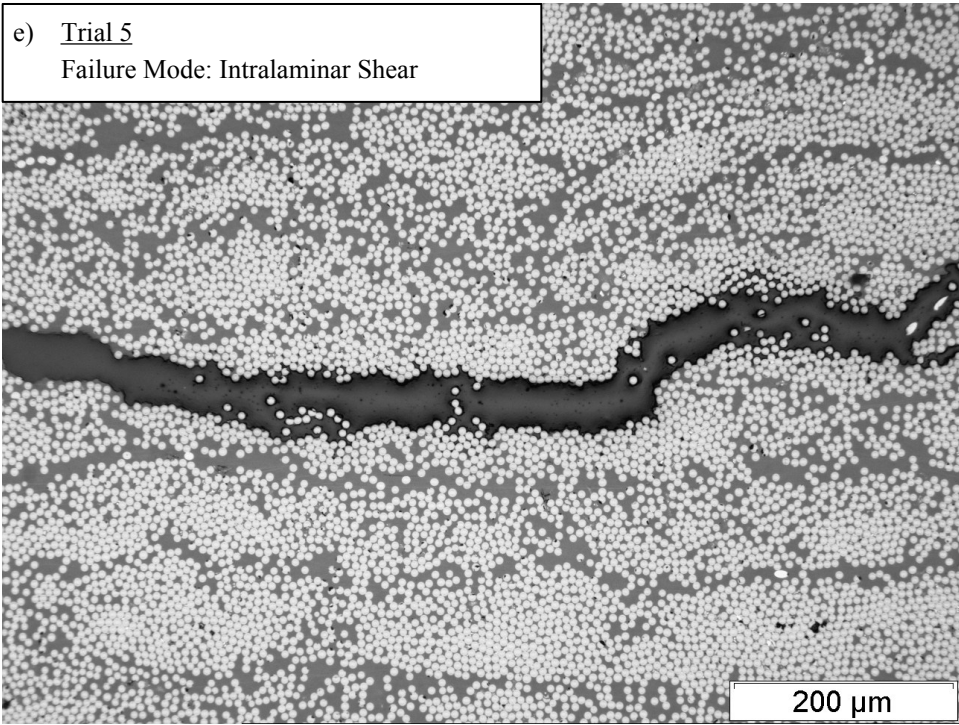
f)   Trial 6
      Failure Mode: Intralaminar Shear

200 µm
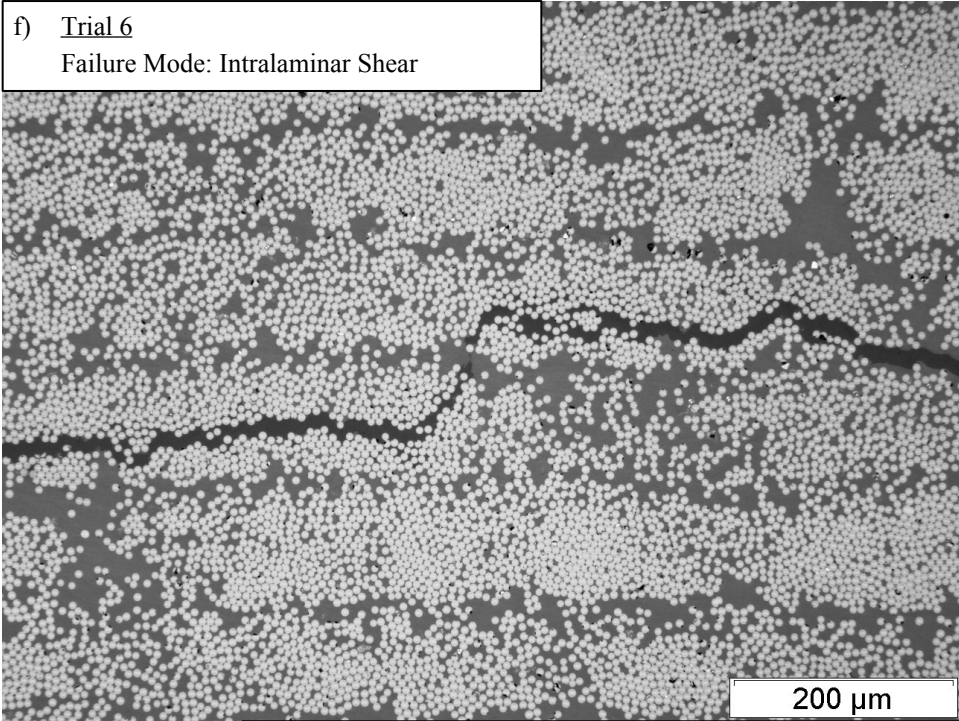
g) Trial 7
    Failure Mode: Intralaminar Shear

200 µm
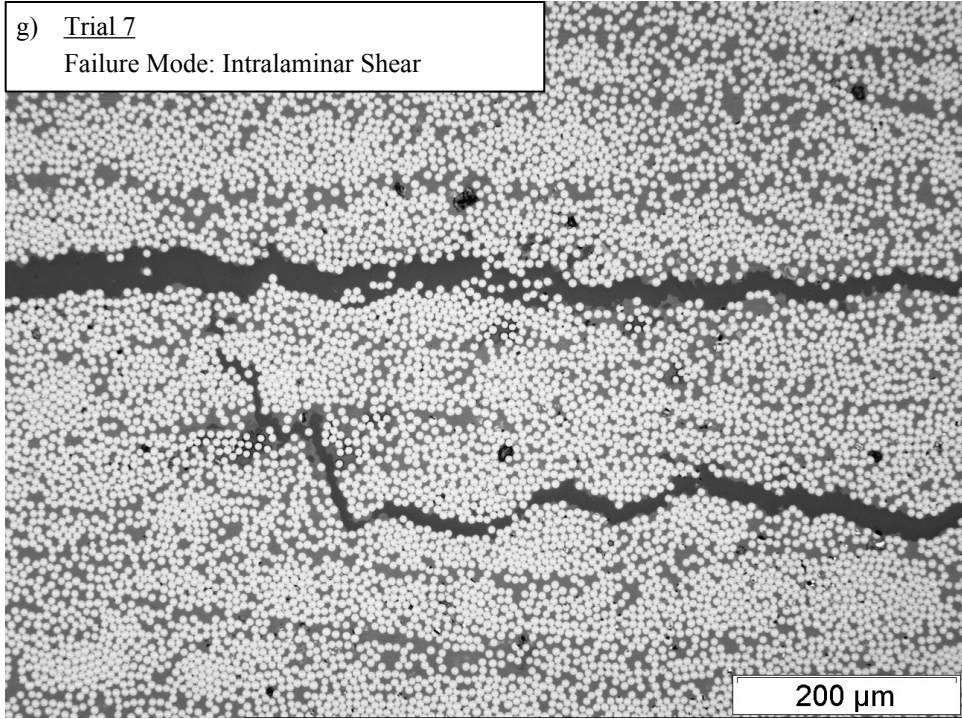
h) Trial 8
    Failure Mode: Intralaminar Shear

200 µm

i) Trial 9
    Failure Mode: Intralaminar Shear

200 µm
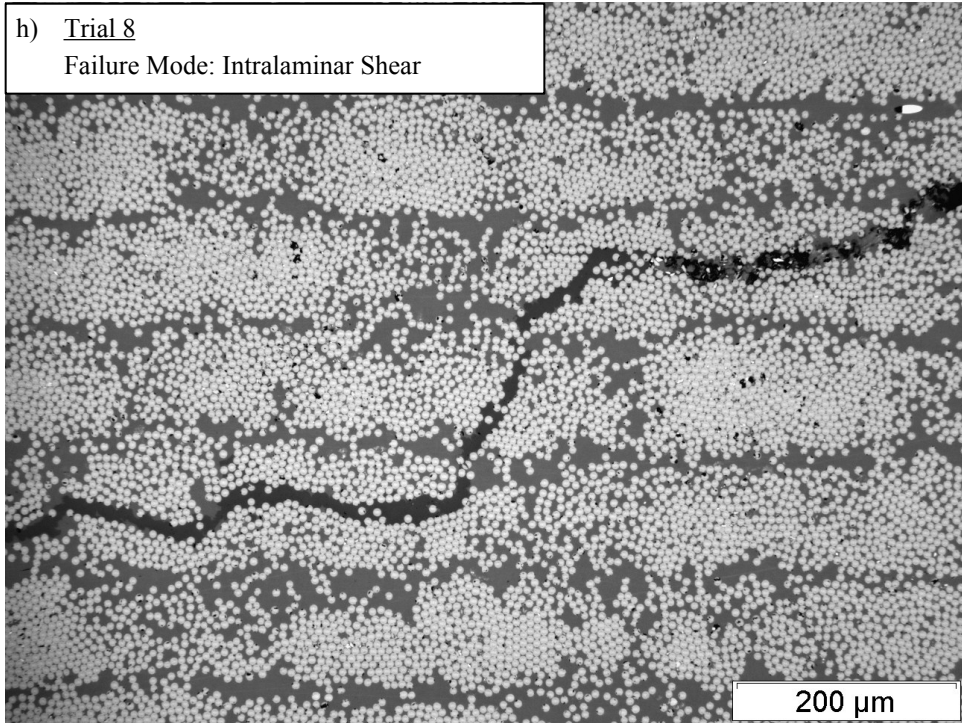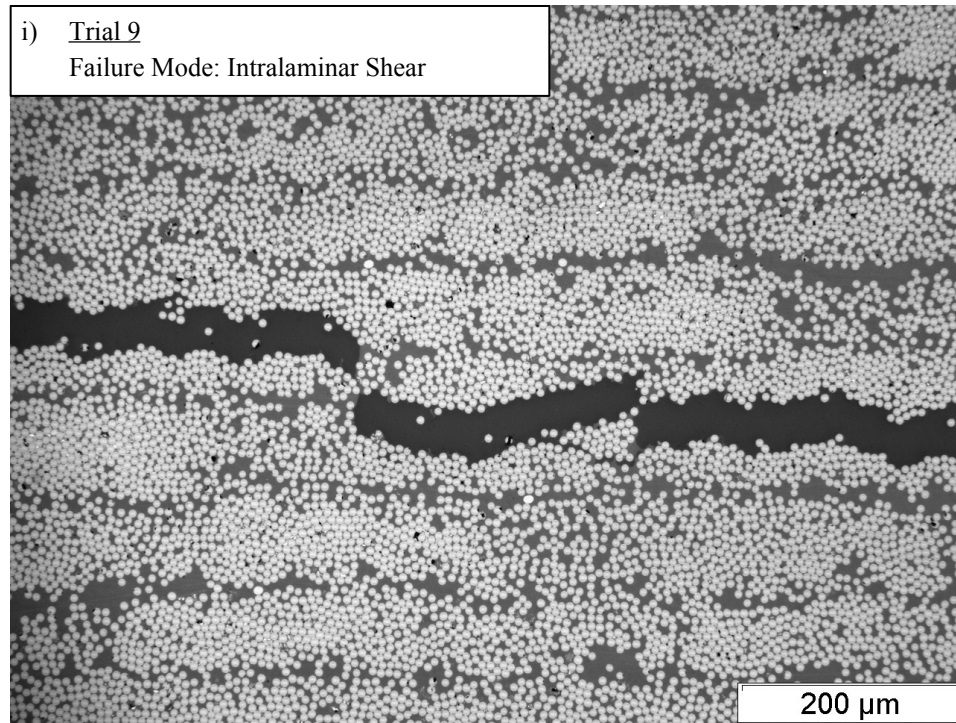
Figure 5.9 Photomicrographs of crack propagation in short-beam specimens

5.5   Statistical Analysis and Discussions

The average effects of four influencing factors are plotted in Figure 5.10a-d. Figure 5.10a shows that the interlaminar shear strength increases with raising the nozzle temperature from 900°C to 925°C, and then deceases if the nozzle temperature continuous to rise. Figure 5.10b suggests that the interlaminar shear strength improves when the process speeds up from 25.4 mm/sec to 50.8 mm/sec; however, the interlaminar strength drops as the process rate increases from 50.8 mm/sec to 76.2 mm/sec. Figure 5.10c indicates that the compaction force has the most significant influence on the interlaminar shear strength among all influencing factors since it has the widest range of values. An improvement in the interlaminar shear strength is observed with the increase of the compaction force by 10 kgf starting from 30 kgf; however, the interlaminar shear strength decreases rapidly if a load of 40 kgf or greater exerts on the incoming tapes.

72

Figure 5.10d shows that the interlaminar shear strength drops slowly when moving the nozzle away from the nip of the compaction roller.

(a) Average Effects of Nozzle Temperature
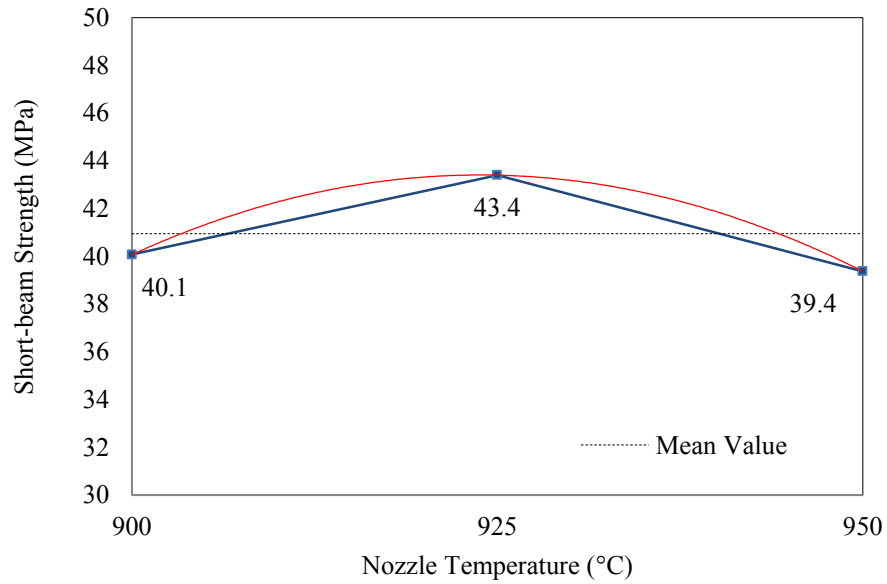
(b) Average Effects of Process Rate
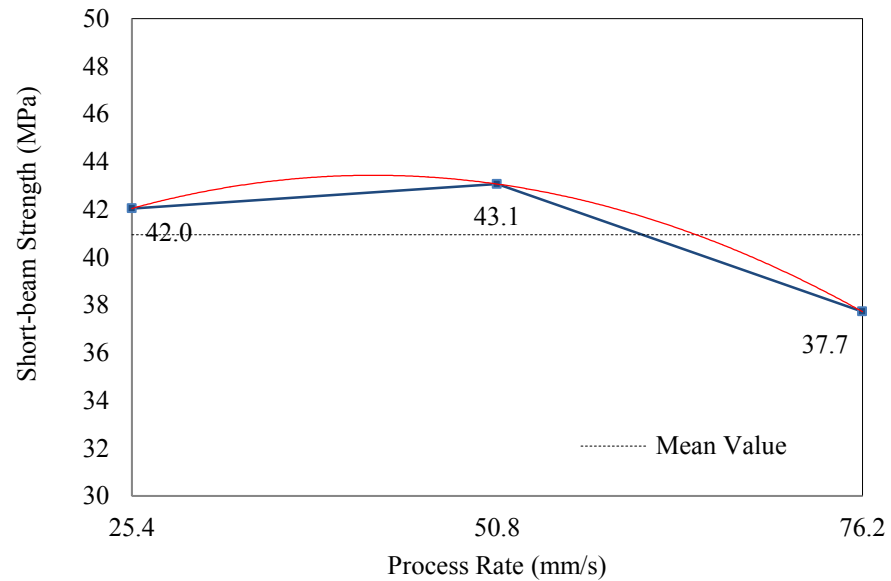
(c) Average Effects of Compaction Force
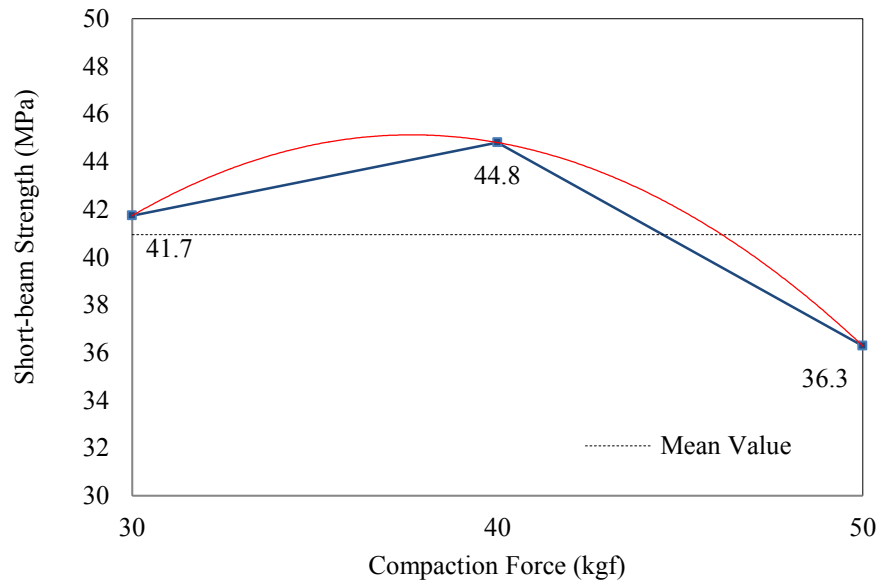
(d) Average Effects of Nozzle Location
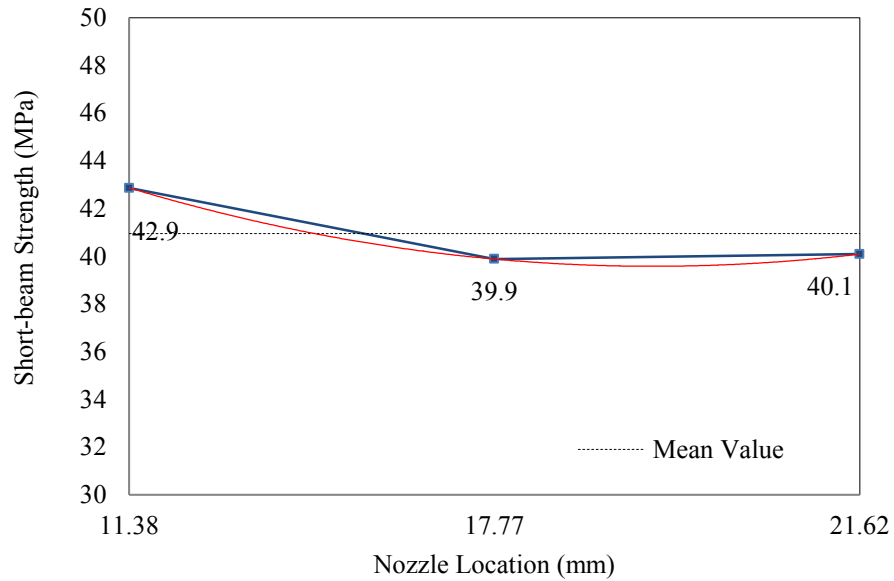
Figure 5.10 Plots of average effects of (a) nozzle temperature, (b) process rate, (c)

compaction force, and (d) nozzle location at three levels

In Table 5.6, the analysis of variance of the experimental results by the Qualiteck-

4 provides the relative influence of factors and interactions on the variability of

experimental results. The main factors influencing the interlaminar shear strength are the nozzle temperature (13.58 %), the process rate (23.63 %), the compaction force (54.66 %), and the nozzle location (8.13 %). It can be concluded that the compaction force has the most significant influence on the interlaminar shear strength. Table 5.7 represents the predictive equation for performance at the optimum condition determined based upon the quality characteristics selected for the analysis. The interlaminar shear strength of a fiber placed composite ring with the optimum process condition would be 51.3 MPa.

Table 5.6 Analysis of variance of experimental results

Factors	DOF	Sum of Sqrs.	Variance	Pure Sum	Percent
Nozzle Temperature	2	27.788	13.894	27.788	13.580
Process Rate	2	48.347	24.173	48.347	23.628
Compaction Force	2	111.843	55.921	111.843	54.659
Nozzle Location	2	16.637	8.318	16.637	8.130

Table 5.7 Optimum process parameters by Taguchi's method

Factors	Level Description	Level	Contribution
Nozzle Temperature	925	2	13.894
Process Rate	50.8	2	24.173
Compaction Force	40	2	55.921
Nozzle Location	11.38	1	8.318
Total Contribution from All Factors			10.353
Current Grand Average of Performance			40.947
Expected Result at Optimum Condition			51.3

CHAPTER 6   Effects of Liquid Environment on Mechanical Performance of Carbon Fiber Reinforced Thermoplastic Stiffened Structures Made Using Automated Fiber Placement

The objectives of this experimental investigation are: (1) to study the influence of liquid environment on mechanical performance of bond strength between an autoclave molded thermoplastic laminate and a fiber placed thermoplastic laminate; (2) to study the moisture absorption characteristic of a fiber placed AS4/APC-2 laminate; (3) to establish a correlation between immersion time, moisture absorption, and mechanical behavior of the single lap joints. To simulate the bond between a fiber placed tailboom skin and a autoclave molded fairlead support frame, two sets of single-lap shear specimens were manufactured by tape placing over the autoclave molded thermoplastic composite panel by diffusion welding. Design considerations were made to ensure that the manufacturing configuration was as similar as possible to a production scenario while accommodating the geometric requirements of the standard test method. The description of each configuration is given in the following section. The weight change as a function of time was measured with samples immersed in (1) distilled water, (2) Aeroshell Fluid 41 mineral hydraulic fluid supplied by Shell, and (3) Jet A supplied by BP. The lap-shear strength was determined with the samples tested in accordance with the standard test method of ASTM D5868 [42].
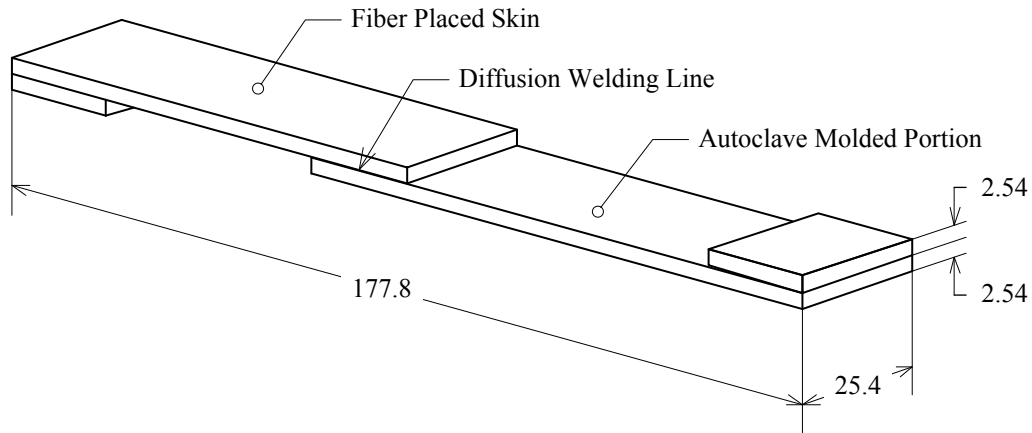
Figure 6.1 Illustration of single-lap shear specimen

6.1   Specimen Fabrication

Both the autoclaved panel and fiber-placed skin were fabricated using AS4/APC-2 unidirectional slit tapes supplied by Cytec. Slit tapes (25.4 mm (1 in) wide) were selected for the fiber placed skin and 304.8 mm (12 in) wide ones for the autoclave molded panel. The first configuration, identified as "0-0", has the fiber direction parallel to the loading direction at the bond interface with the layup sequence of $[(0/90/\pm45)_2/0]_S$ for both autoclave molded and fiber placed halves. The second configuration, identified as "90-90", has the fiber direction perpendicular to the loading direction at the bond interface with the layup sequence of $[(90/0/\pm45)_2/90]_S$ for both the autoclave molded and fiber placed halves.

First of all, a series of flat panels were fabricated via hand layup followed by the autoclave molding process. The tool was prepared by cleaning it thoroughly with acetone followed by three coats of Frekote NC-44 on all surfaces that would be in contact with the composite material. Kapton film was placed on the top and bottom of the laminate to ensure the mirror surface finish (see Figure 6.2a). Once the tool was ready and the plies precut, the laminate was placed into the tooling (see Figure 6.2b). A caul plate was used

to ensure even pressure distribution (Figure 6.2c). Without a caul plate, the vacuum bag can sometimes settle unevenly and create both localized surface defects as well as unacceptable global variations in thickness. Thermocouples were inserted into the edges of the laminate so that the actual part temperature could be monitored during the autoclave molding process (see Figure 6.2d). Glass matting was wrapped around the corners of the tool (see Figure 6.2e) to protect the vacuum bag from damage. As Kapton film has poor flexibility, any unsupported bridge of film formed by the vertical edge of the frame and horizontal surface of the base plate in the corner has a high probability of failure. Glass matting fills these voids and helps to prevent bag failure. High temperature sealant tape was applied to the edges of the base plate and the Kapton bagging film was laid over the assembly. Four pleats were distributed on the edges to create slack in the bag to accommodate the height of the tool (see Figure 6.2f and Figure 6.2g). A steel frame was fastened through the sealant tape to ensure a proper seal, and the bag was pressure tested (see Figure 6.2h). The tooling was placed into the autoclave and processed according to the recommended processing cycle as shown in Figure 4.8. The final panels were unbagged and water jet cut to the required dimensions.

| a) clean and treat tool | b) cut and stack plies |

c) install caul plate and thermocouple

d) protect frame edges

e) cover glass matting

f) apply bagging film

g) install tool frame

h) test vacuum bag
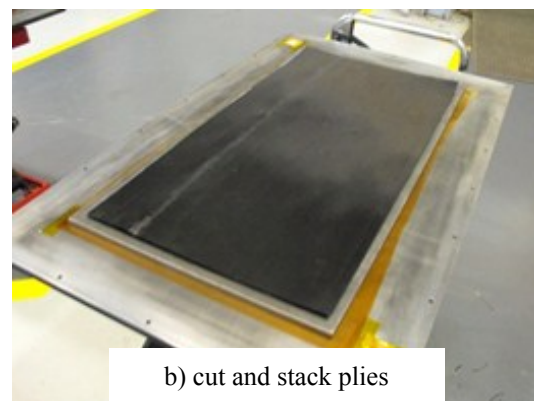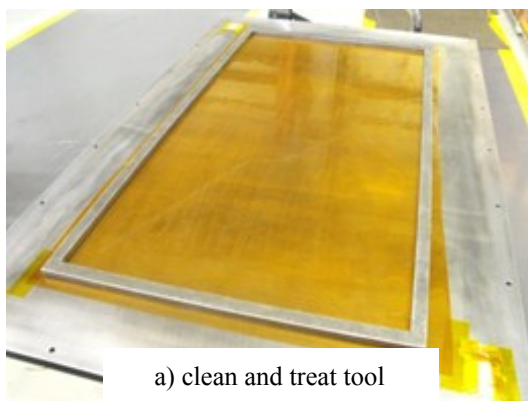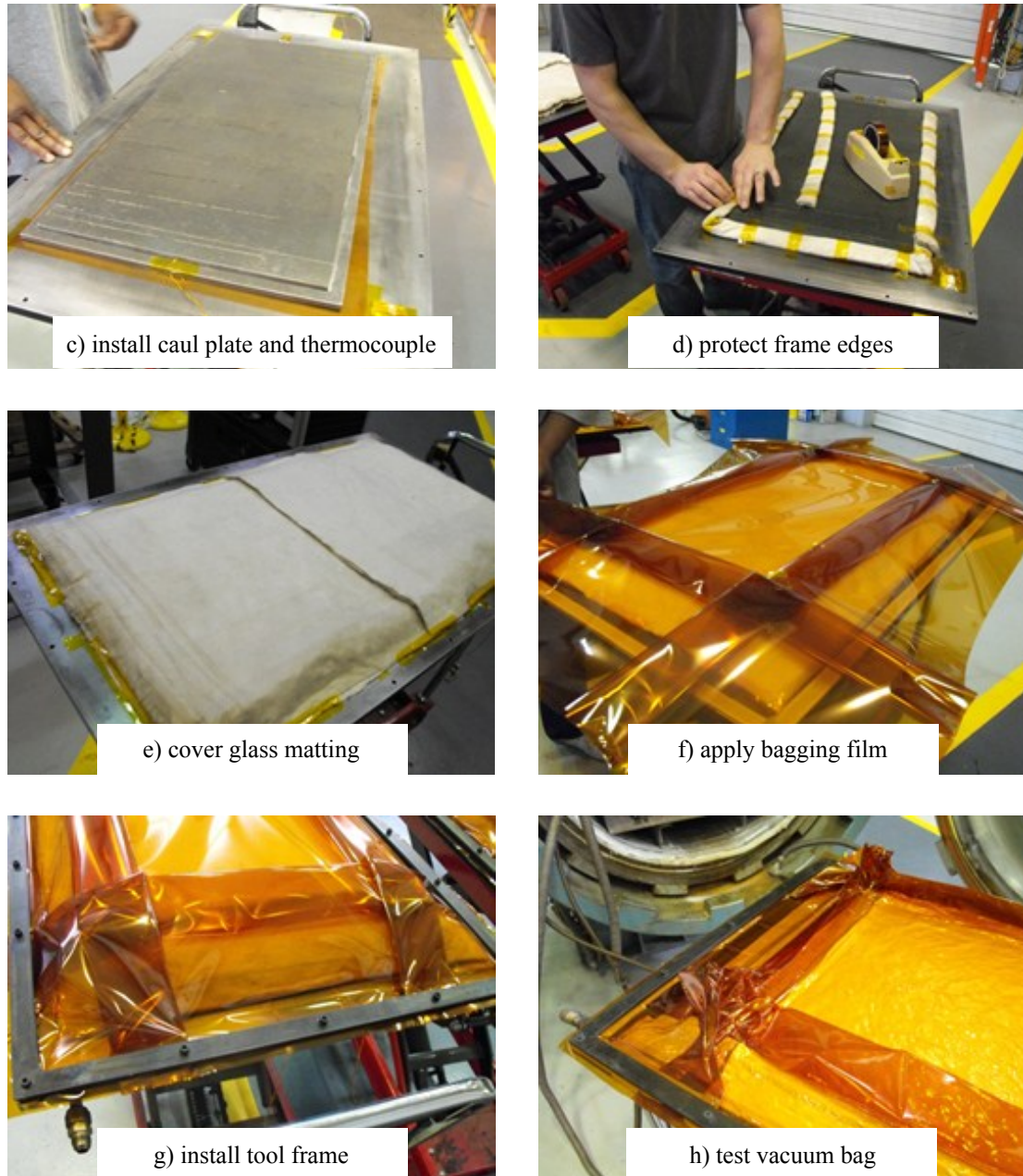
Figure 6.2 Procedure of assembling vacuum bag

Once complete, the autoclave molded panels were scuffed with an abrasive cleaning pad and cleaned thoroughly with acetone and ether. To improve efficiency, the coupons were fabricated in panels with two mirrored rows of coupons. The autoclave molded panels were arranged with aluminum spacers on a flat surface. The spacers define one edge of the bond area. The other is defined by a 0.076 mm (0.003 in) thick strip of

stainless steel shim, also coated with Frekote 44-NC. The robotic fiber placement system equipped with the dual-torch heating system shown in Figure 6.3 was employed to place the materials over the tool surface illustrated in Figure 6.4. In addition, a compaction roller was heated up with an electrically resistant heating element that inputs additional thermal energy during diffusion bonding. In total, two different panels were fabricated using the processing condition as follows:

Nozzle Temperature = 975 °C; Process Rate = 76.2 mm/sec;

Compaction Force = 136 kgf; and Roller Temperature = 475 °C.

Figure 6.3 Dual-torch automated fiber placement system (photo courtesy of Automated Dynamics)

After the fiber placement process, the aluminum spacers were removed and the individual coupons were water jet cut from the panel to the dimensions as shown in Figure 6.5. The spacing created by the aluminum spacer as well as the captured stainless steel shim between the autoclaved panel and the fiber placed skin are shown in Figure 6.6a. In order to prevent damage to the autoclaved panel, the diamond cutter only cut to within 0.015" of the shim stock. The remainder was removed using a utility knife as shown in Figure 6.6b. The waste portion and stainless steel shim was then removed completely as shown in Figure 6.6c. The coupons were scribed with a unique serial number and were then complete.
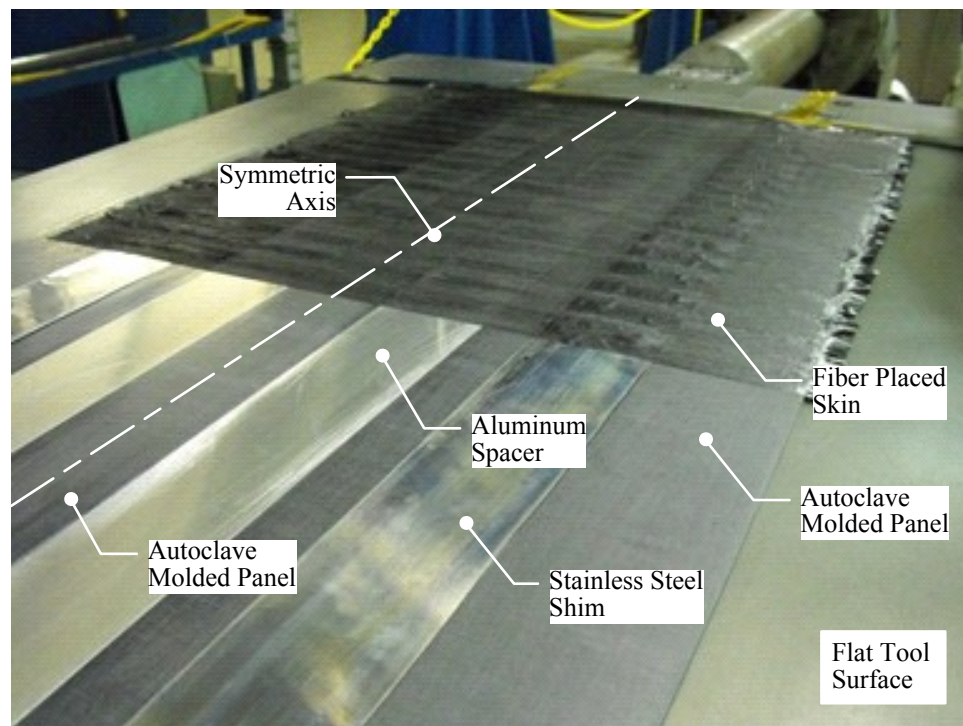
Figure 6.4 Illustration of tooling for manufacturing test coupons
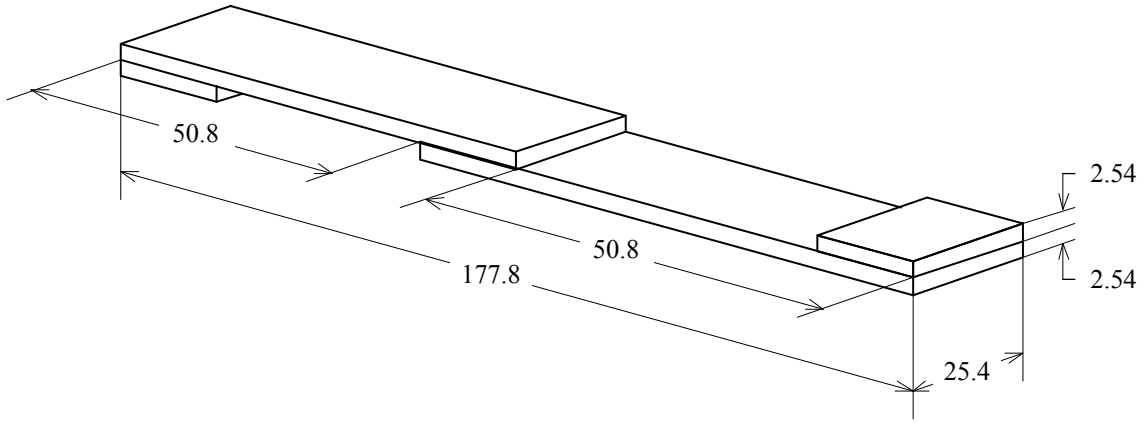
Figure 6.5. Specimen configurations for single-lap shear test

a)

Fiber Placeed Portion

Autoclave Molded Portion

Stainless Steel Shim

b)

Fiber Placeed Portion

Autoclave Molded Portion

Stainless Steel Shim

c)

Fiber Placeed Portion

Autoclave Molded Portion
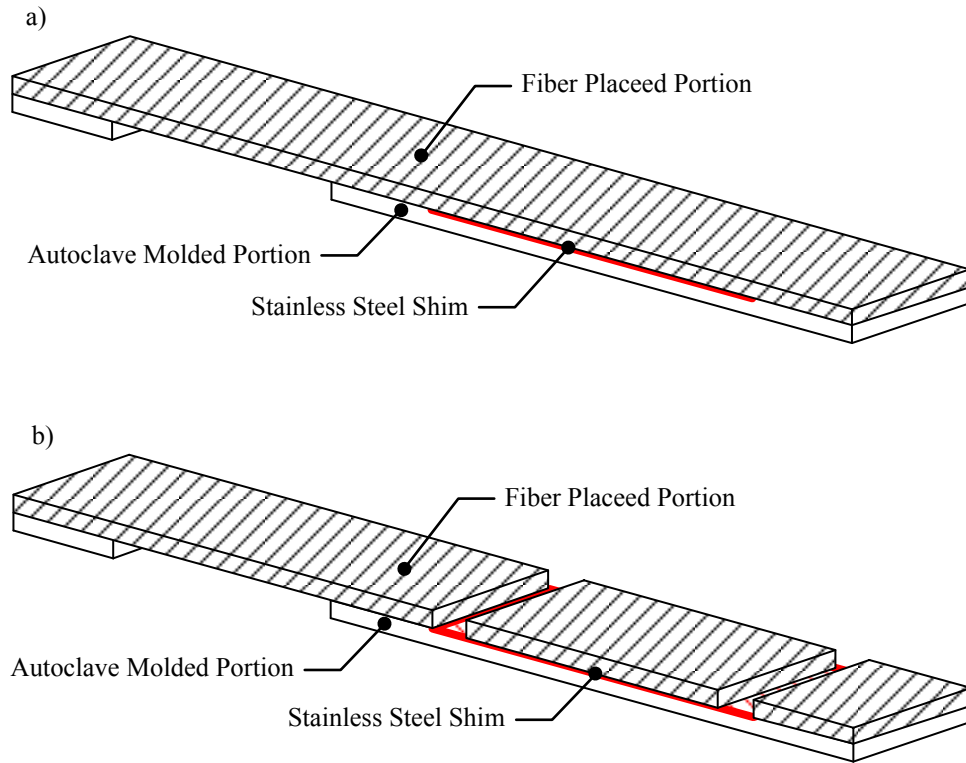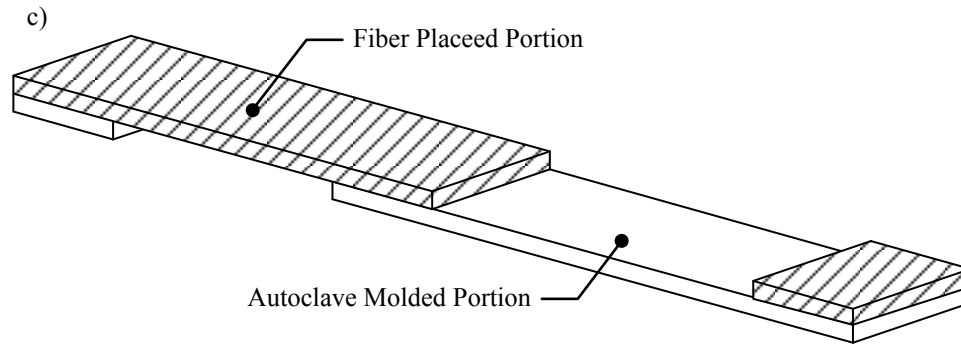
Figure 6.6 Specimen preparation: a) cut coupon with captured stainless steel shim by a water jet cutter; b) slot coupon via a diamond bladed cutter; c) remove remainder and stainless steel shim.

6.2   Specimen Inspection

6.2.1   Dimensions

The completed coupons were inspected for geometric accuracy and laminate quality in accordance with the standard test method. It was noticed that the fiber placed part of the specimens was curved up in the long direction of the specimen as shown in Figure 6.7. This is likely a function of the pre-stress that is preserved in each ply as it is placed via the in-situ process. Unreinforced composite structures that are autoclave cured have more distributed pre-stress and generally maintain more flat open section profiles.
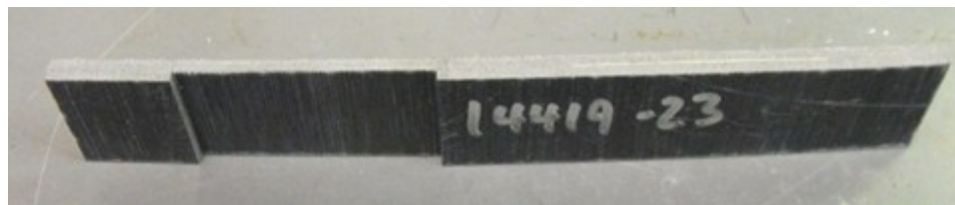
Figure 6.7 Illustration of curved up specimen

6.2.2   Microscopy

Two test coupons were sectioned, mounted and polished to examine the laminate quality in details. They were cut using a diamond bladed saw in such a way that the

surface of interest was perpendicular to the bonding interface of plies. This prevents fiber pull-out during the polishing procedure at the bond interface which would obscure the bond quality. The samples were cast using a low viscosity, optically clear two part epoxy casting resin under normal atmosphere in order to prevent the filling of voids in the laminate. A six-step grinding and polishing procedure was followed to prepare the surface of the cast specimens. Digital photomicrographs were captured using a Leitz optical microscope and Olympus DP70 camera with included software.

6.2.3 X-Ray Microtomography

X-ray microtomography (or Micro-CT) was employed to obtain three-dimensional microstructural information about a diffusion bonded laminate, which has been recently used in composite research to characterize woven fabric composite and detect internal damage of composite structures [43-48]. A sample nominally 6.35 mm by 6.35 mm was cut from the center of a 0-0 configuration specimen. Prior to scanning, the sample was mounted in a grip consisting of a Styrofoam block with a slot on one side and a machined hole on the other. The slot held the sample in place with minimal contact and pressure while the hole allowed easy but tight placement onto a copper mounting rod. Skyscan's 1172 High-Resolution Micro-CT was used for scanning. Skyscan's NRecon software was then used to reconstruct the raw shadow projections into sets of parallel X-ray micrographs. All reconstruction settings were kept constant with the exception of the post-alignment, which was adjusted for each sample for maximum clarity.

6.3 Specimen Conditioning

Before placing the specimens into the distilled water, hydraulic fluid, and jet fuel, the specimens were dried in an oven at 50 °C until no more weight loss was observed.

The dry specimens were then weighed on a Mettler 200 analytical balance. The hydraulic fluid selected for this investigation is Aeroshell Fluid 41 mineral hydraulic fluid supplied by Shell and the jet fuel is Jet-A supplied by BP with anti-icing additives. The oven-dry specimens were then placed into unstirred water baths supplied by VWR International at a temperature of 50°C ± 1°C for 1389 hours. The specimens were spaced parallel, 6.35mm apart in the baths, and the distance between coupon edges and the water bath and the liquid surface was 25mm. At the end of the period, specimens were removed from the water baths one at a time, wiped free of surface moisture with a dry cloth, and weighed on the analytical scale.

6.4 Moisture Absorption

The ASTM D5229 test standard was adopted for the determination of moisture absorption in the test coupons. The amount of the moisture absorption as a function of time was measured according to percentage increase in weight [49].

$$M(t) = \left[\frac{m(t) - m_{Dry}}{m_{Dry}} \right] \times 100 \tag{6.1}$$

where m_{Dry} is the oven-dry mass of the specimen, $m(t)$ is the mass of the specimen after immersion for time t and $M(t)$ is the percent moisture content of the specimen as a function of time.

6.5 Single Lap Shear Test

The lap shear test was adopted in this study since it is the widely used method for evaluating the in-situ shear strength on adhesively bonded joints due to its simplicity and low costs associated with specimen fabrication, testing, and data analysis. The conditioned specimens were tested under uni-axial tension on a MTS axial servo-

hydraulic test system per ASTM D5868 [42]. The test system was equipped with an axial load cell with the force capacity of 100 kN. The specimens were aligned with the assistance of a pair of L-shaped brackets mounted on the upper and lower wedges. Subsequently, they were loaded axially at the rate of 13 mm/min until failure occurred. Five specimens in each case were tested. The average lap shear strengths were calculated as the load applied to the joint divided by the bond area. The failure modes were recorded per the ASTM D5573 test standard [50].

$$\tau_{Avg} = \frac{P}{w \times l} \tag{6.2}$$

where P is the ultimate load at failure, w is the width of the specimen, and l is the length of the bond line.

6.6   Experimental Results and Discussions

Figure 6.8 shows the flat test panel was warped after removing it from the tool surface owing to the relief of the residual stress. This is a common issue associated with the manufacturing of flat thermoplastic composite panels using the in-situ consolidation technique. The process-induced residual stress influences the dimensional stability of the fiber placed panel but also its mechanical performance in service.
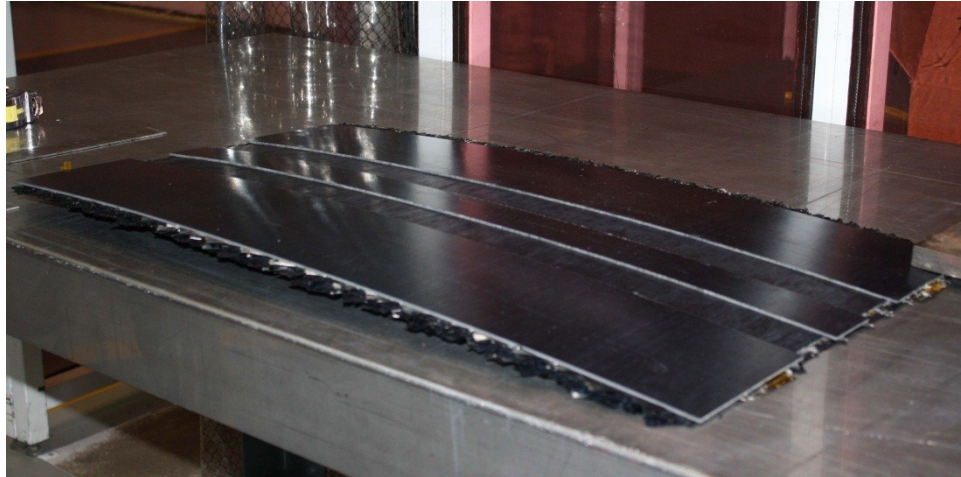
Figure 6.8 Illustration of warped test panel after fiber placement

Figure 6.9 shows that the resulting laminate quality at the bond interface is indistinguishable from the fiber placed material. However, the photomicrograph of the polished cross-section of a 0-0 specimen seems to be ineffective for locating void and evaluating its volume fraction. During the polishing process, a small amount of carbon fibers parallel to the polished surface might be pulled out or broken off from the sample due to low ductility. The darkened shadow may not be the void resulting from the fiber placement process. Therefore, Micro-CT was implemented to examine the void distribution in the interior of the sample as the supplement to optical microscopy. Figure 6.10 demonstrates that the fiber placed portion exhibits a higher void content than the autoclave molded portion. There are a considerable amount of voids at the bond interface. Interestingly, most voids seem to be aligned and alternated through the thickness of the fiber placed portion. The porosity analysis performed by CT Analyzer shows that the void content is 1.65 % for the fiber placed portion as compared to 0.01 % for the autoclave molded portion. Although the Micro-CT is capable of examining the distribution of voids with the size of 3 μm or greater, it cannot differentiate AS4 from APC-2 due to their similar density.

Figure 6.9 Photomicrograph of polished cross-section of an unconditioned 0-0 test

coupon
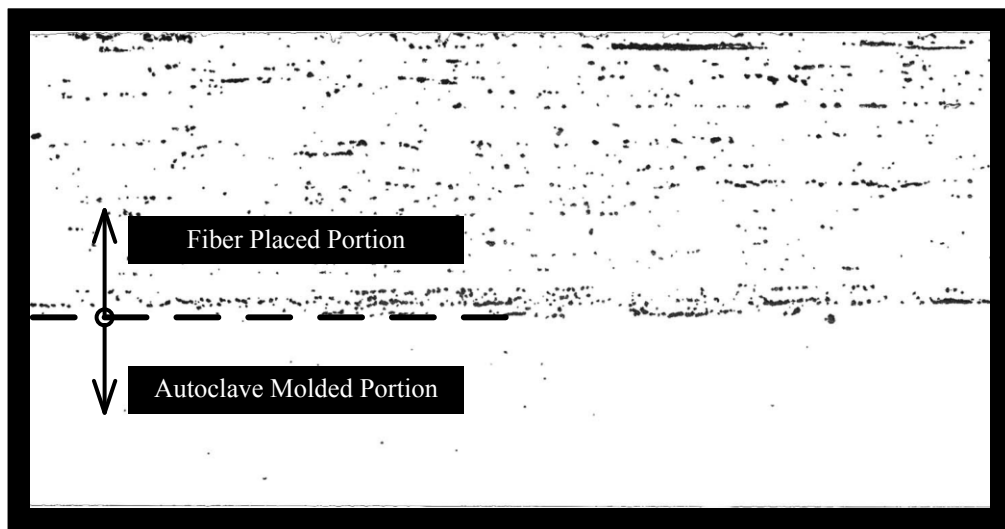
Figure 6.10 Three-dimensional X-ray photomicroscope of the cross-section of autoclave

molded and fiber placed laminates

Figure 6.11 shows the average weight gain of the conditioned specimens. The average weight of oven-dry 0-0 and 90-90 lap-joint specimens were measured at 24.52 g and 25.10 g respectively. Over the course of the experiment, 0-0 and 90-90 specimens immersed in distilled water at 50°C gain 0.40 % and 0.85 % of their body weight. 0-0 and 90-90 specimens conditioned in the hydraulic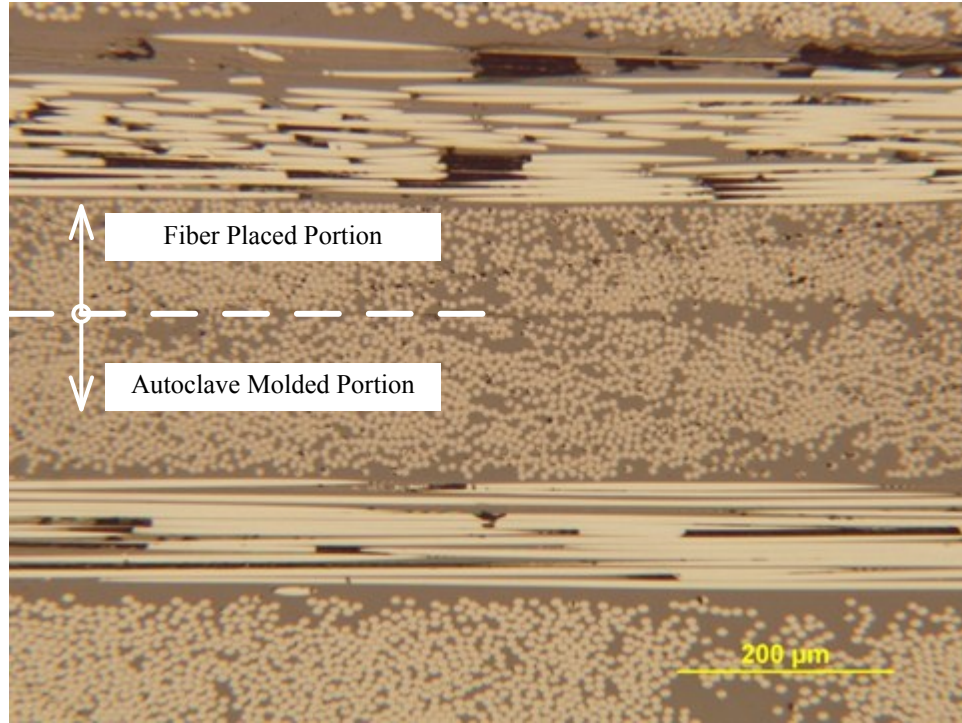 fluid at 50°C gain 0.94 % and 1.43 % of their body weight. 0-0 and 90-90 specimens immersed in the jet fuel at the ambient temperature gain 1.61 % and 2.31 % of their body weight. The experimental results show that the jet fuel has the highest fluid absorption among all media. Additionally, 90-90 specimens exhibit approximately twice the fluid absorption as the 0-0 ones as there are more cut fiber ends exposed in the 90-90 specimens than the 0-0 ones. Cut fiber ends are more prone to absorbing fluids than the as-processed surface of the part or fibers only tangentially cut. Visual inspection during the conditioning process shows no signs of discoloration or chemical degradation on the surfaces of specimens. It implies that no chemical or physical changes have occurred in the conditioning process. The plot shows that the conditioning time is not sufficient for reaching the equilibrium of the specimens immersed in any media. Mahieux, Lehmann, and desLigneris [51] show that the moisture absorption of water and industrial oil is negligible for the press molded AS4/APC-2 laminates which is contradictory to the experimental results obtained in this investigation. However, it would be expected that fiber placed laminates have higher moisture uptake due to the micro-size voids which prompt the penetration of fluids into a porous structure.
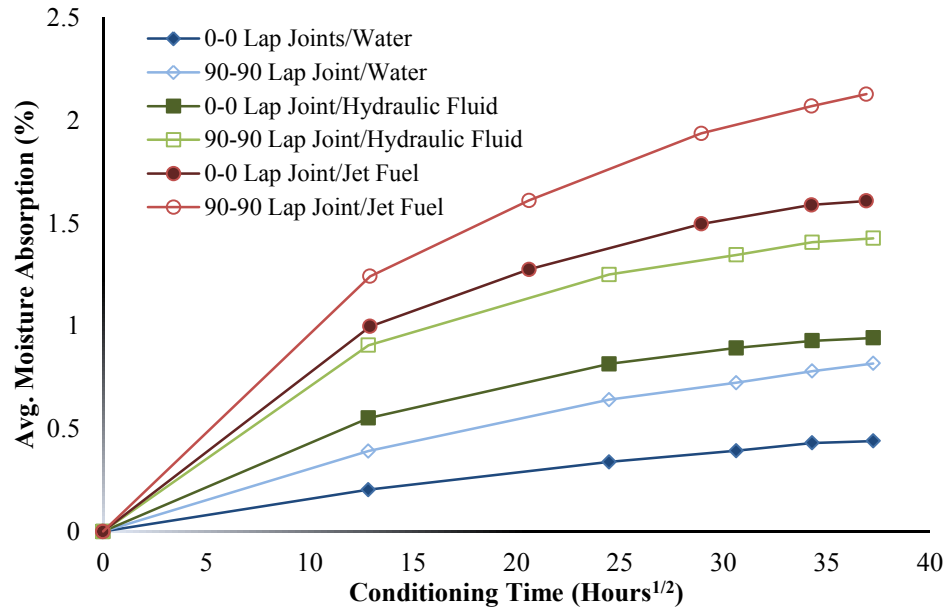
Figure 6.11 Average moisture absorption as a function of time

The average lap shear strengths for unconditioned and conditioned specimens are plotted in Figure 6.12 and Figure 6.13. The experimental results show that the bond strength for two 0° plies meeting at the bond interface has a higher load than that of two 90° plies meeting at the bond interface. It can be explained that the carbon fibers in 0-0 specimens take a fraction of applied loads during testing. The lap shear strength for the specimens conditioned in the hot water almost remains unchanged. The lap shear strength for 0-0 and 90-90 specimens conditioned in hydraulic oil drops at 12.81 % and 4.72% respectively.
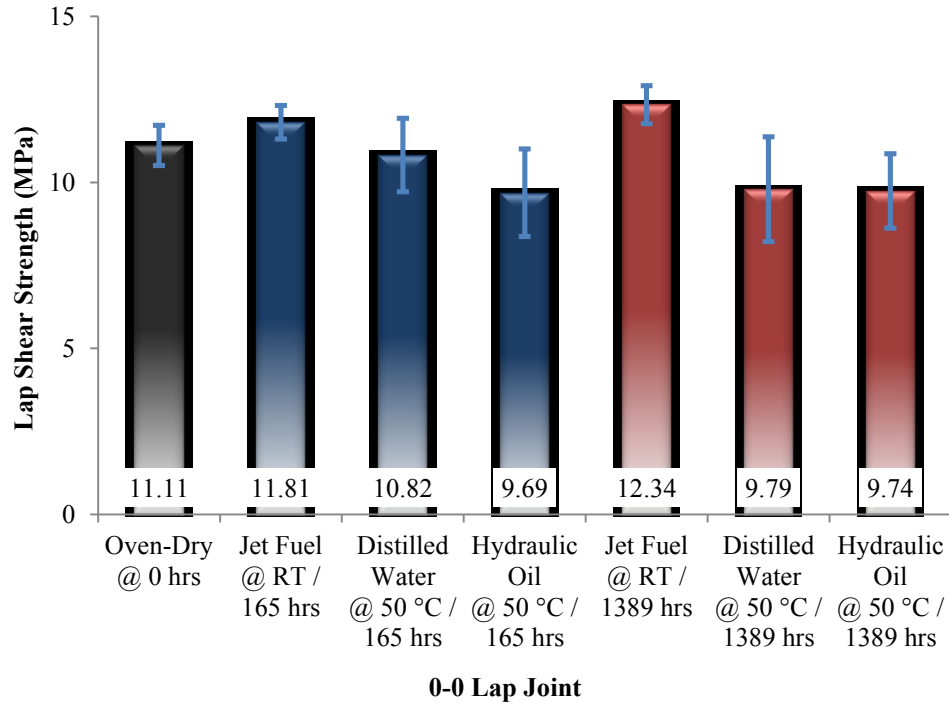
Figure 6.12 Lap shear strength for 0-0 conditioned test coupons
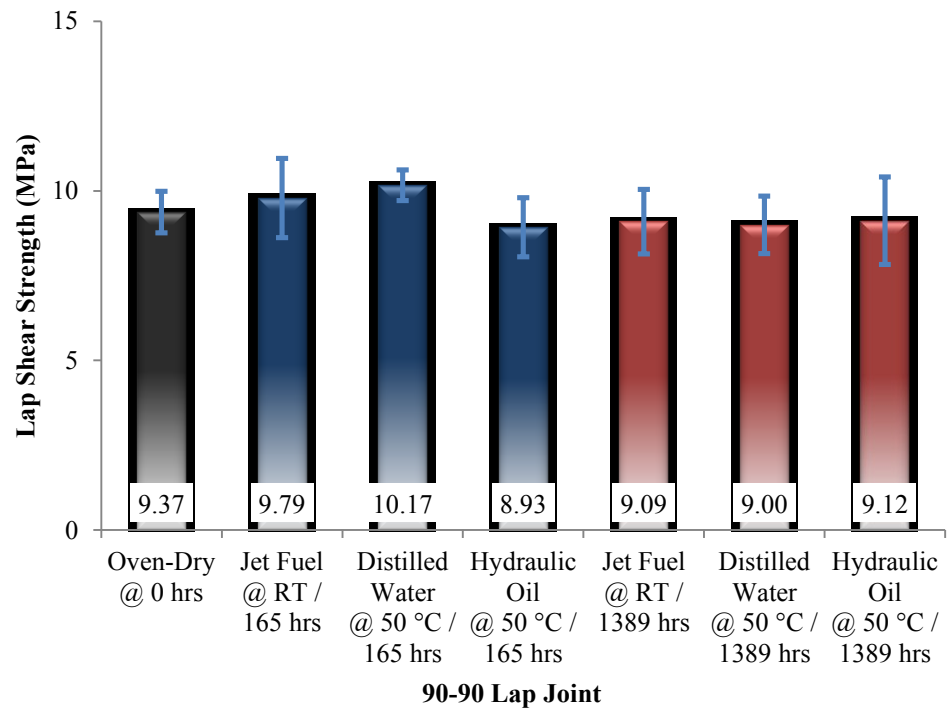
Figure 6.13 Lap-hear strength for 90-90 unconditioned and conditioned test coupons

Scanning electron microscopy (SEM) was used to examine the fracture surface on the fiber placed side since all specimens failed at the fiber placed halves. Figure 6.14 shows the fracture surface of an unconditioned 0-0 specimen after testing. The failure mode is identified as the fiber-tear failure occurring within the matrix in the fiber placed portion, characterized by the appearance of carbon fibers on both rupture surfaces. Figure 6.14 to Figure 6.16 reveal that the voids in the fiber placed part tend to align with the fiber direction within plies rather than bond lines. Figure 6.16 illustrates that the matrix failed to fill up the void during processing.

It must be pointed out that as expected the lap-shear strength obtained in the study is much lower than that obtained by other researchers. For example, Maguire [52] obtained a lap shear strength of about 40 MPa with the vibration welding process, with an extra PEEK film placed in the joint, and Sliverman and Griese [53] and Xiao, Hoa and Street [54] reported lap shear strengths of about 25 MPa with the electrical resistance welding process. The reduction in lap shear strengths is considered to be due to the combined effects of specimen warpage and micro-size voids. First, normal stresses resulting from the specimen warpage in the fiber placed portion, in combination with the applied shear stress, significantly lowers the lap-shear strengths. Second, the voids within the fiber placed portion serves as the crack initiating points which promotes premature failures during testing. It is inferred that the testing setup and processing parameters have to be re-evaluated to minimize the void content and eliminate the unexpected warpage on the fiber placed side. As a result, it is not recommended to build the tailboom skin on the pre-consolidated fairlead support frames using these process parameters. Optimum process parameters have to be determined experimentally.

Figure 6.14 SEM micrograph of fracture surface of unconditioned 0-0 configure coupon

after failure at the magnification of 50X
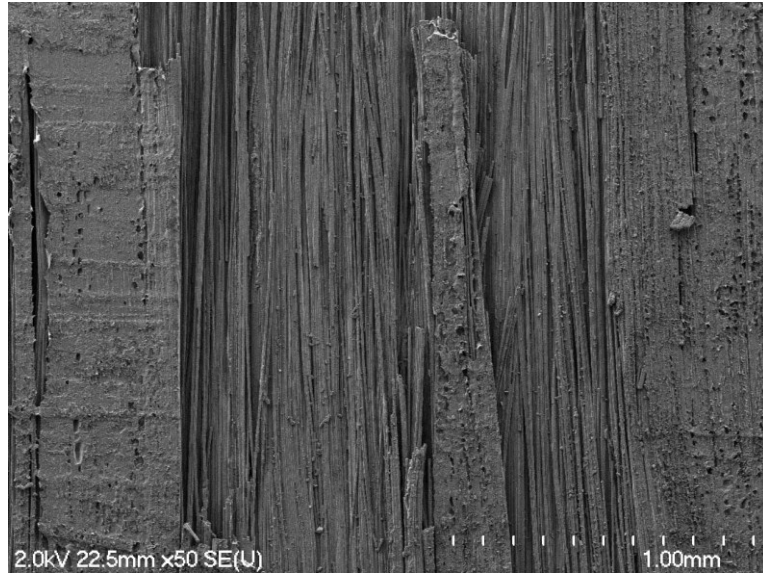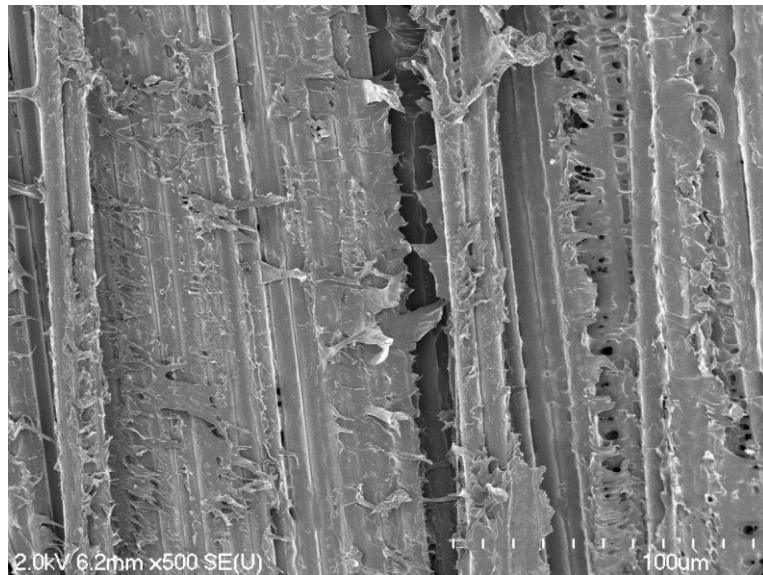

Figure 6.15 SEM micrograph of fracture surface of unconditioned 0-0 configure coupon

after failure at the magnification of 500X
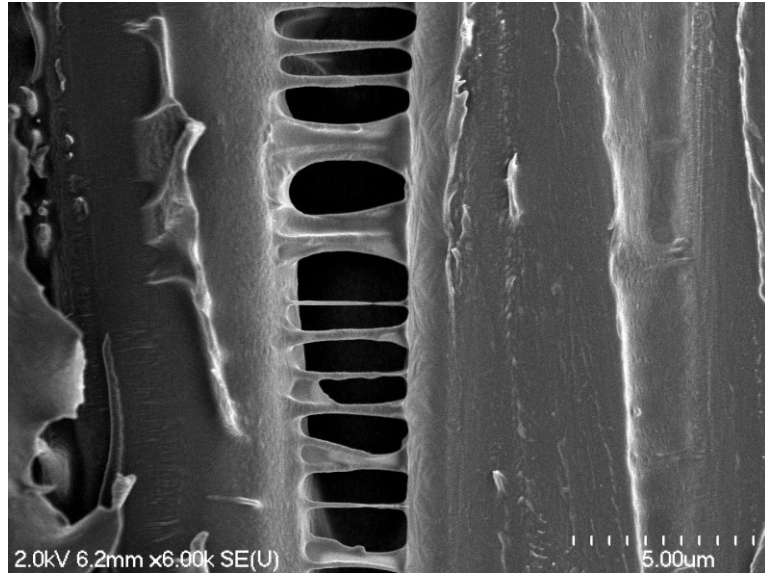
Figure 6.16 SEM micrograph of fracture surface of unconditioned 0-0 configure coupon

after failure at the magnification of 6000X

CHAPTER 7 Conclusions

Conclusions drawn from the research work presented in the previous chapters are summarized as follows:

1. From the modeling it was found that when adding more sections to the conical surface, the percentage of lap increases linearly and the angular deviation of fiber orientation drops exponentially. The optimum fiber path design for the manufacturing of the demonstration articles is to divide the tool surface into two equal sections for ±45° plies and four equal sections for 0° plies. The radius of the compaction roller is 407.49 mm (16.043 in) for ±45° plies and 187.17 mm (7.369 in) for 0° plies to provide the optimum compaction load distribution. The flat compaction roller is used for 90° plies.

2. Interlaminar defects have minimal effects on tensile, compressive, and shear properties of the autoclave molded thermoplastic composite laminates containing one 6.35 mm (0.25 in) wide gap or lap. These defects cause the out-of-plane waviness on adjacent plies, which reduces the compression strength of the laminates in the transverse direction as reported. Photomicrographs show that the plies adjacent to those defects are stretched to compensate the geometric variations.

3. It can be concluded that the quality of fiber placed laminates depends on the processing parameters set to the fiber placement system. Moreover, the compaction force has the greatest impact on the strength properties of the fiber placed laminates. Under the horizontal shear load, fiber placed specimens behave differently from autoclave molded specimens. Specifically, cracks initiate and

propagate within individual plies instead of at bond interfaces. This implies that the bond strength at the interface of two adjacent plies is better than that in between fibers and matrix. The presence of a large amount of micro-scale voids in between fibers accounts for the reduction of short-beam strength. The optimum process condition for manufacturing AS4/APC-2 on the automated fiber placement system is given as:

Nozzle Temperature $= 925\ °C$;

Process Rate $= 50.8$ mm/s;

Compaction Force $= 40$ kgf;

Nozzle Location to Nip Point $= 11.38$ mm.

4. The lap shear strengths of the test coupons obtained from the experiments are much lower than these reported in the open literature due to specimen warpage and micro-size voids. The fluid absorption was greatest for the set of specimens immersed in the jet fuel at the ambient temperature. 90-90 specimens exhibited approximately twice the mass uptake as the 0-0 ones due to more exposed fiber ends in 0-0 specimens. However, 0-0 specimens are capable of taking higher shear loads than 90-90 ones, where the fibers at the interface take a fraction of the applied load. Specifically, the lap shear strengths of 0-0 and 90-90 test coupons immersed in hydraulic oil drop 17.9 % and 4.7 % respectively. The photomicrographs reveal that most voids are located in between fibers within individual plies which result in a reduction in lap shear strength.

CHAPTER 8   Future Work

High priority is given to research on the fabrication of flat thermoplastic composite panels by the in-situ fiber placement technique for determining the strength and stiffness properties of fiber placed laminates and comparing these of autoclave molded laminates. It is concluded that the current manufacturing methodology is problematic in minimizing excessive process-induced residual stresses during processing. A great challenge for researchers is to control the residual stresses and the stresses distribution of each ply. Moreover, a study of the laser heating system as a substitution of the high temperature gas torch installed in the work cell is desired to improve the process rate and minimize imperfections resulting from the use of electrically resistant heating elements in the hot gas torch.

References

[1]   Boeing. (02/20). *787 Dreamliner program fact sheet*. Available:

http://www.boeing.com/commercial/787family/programfacts.html

[2]   Airbus. (02/20). *A350 XWB technology*. Available:

http://www.airbus.com/aircraftfamilies/passengeraircraft/a350xwbfamily/technolo
gy-and-innovation/

[3]   IAPD. (2010) Thermoplastic composites for aerospace. *The IAPD Magazine*.

[4]   J. Hale. (2009) Boeing 787 from the ground up. *AERO*. 8. Available:

http://www.boeing.com/commercial/aeromagazine/articles/qtr_4_06/article_04_2.
html

[5]   S. Béland, *High performance thermoplastic resins and their composites*: Noyes
Data Corp., 1990.

[6]   K. E. Tessnow, J. G. Hutchins, D. G. Carlson, and M. J. Pasanen, "Low-cost
thermoplastic helicopter tailboom development," 1994.

[7]   W. E. Moddeman, W. C. Bowling, E. E. Tibbitts, and R. B. Whitaker, "Thermal
stability and compatibility of polyetheretherketone (PEEK) with an oxidizer and
pyrotechnic blend," *Polymer Engineering and Science,* vol. 26, pp. 1469-1477,
1986.

[8]   M. Day, J. D. Cooney, and D. M. Wiles, "Thermal stability of poly(aryl-ether-
ether-ketone) as assessed by thermogravimetry," *Journal of Applied Polymer
Science,* vol. 38, pp. 323-337, 1989.

[9]   B. Shirizadeh, F. Chee Wei, and T. Boon Hui, "Robotic fibre placement process
planning and control," *Assembly Automation,* vol. 20, pp. 313-20, 2000.

[10]   T. C. Anderson, "Low-cost composite tailboom," *Collection of Technical Papers -
AIAA/ASME/ASCE/AHS/ASC Structures, Structural Dynamics and Materials
Conference,* vol. 3, pp. 2026-2035, 1999.

[11]   C. Marsden, R. Fews, P. Oldroyd, and A. Yousefpour, "Design for manufacturing
– one-piece, fibre-placed composite helicopter tailboom," *IOP Conference Series:
Materials Science and Engineering,* vol. 26, p. 012016, 2011.

[12]   C. Quinn. (2012). *Innovative low-cost, in-situ consolidation head for complex
geometry thermoplastic fiber placement*. Available:
http://www.virtualacquisitionshowcase.com/browse/popup/1629

[13]   E. L. Wang and T. G. Gutowski, "Laps and gaps in thermoplastic composites
processing," *Composites Manufacturing,* vol. 2, pp. 69-78, 1991.

[14]   A. J. Sawicki and P. J. Minguet, "Effect of intraply overlaps and gaps upon the
compression strength of composite laminates," in *Proceedings of the 1998 39th
AIAA/ASME/ASCE/AHS/ASC Structures, Structural Dynamics, and Materials
Conference and Exhibit and AIAA/ASME/AHS Adaptive Structures Forum. Part 1
(of 4), April 20, 1998 - April 23, 1998*, Long Beach, CA, USA, 1998, pp. 744-754.

[15]   K. Croft, L. Lessard, D. Pasini, M. Hojjati, J. Chen, and A. Yousefpour,
"Experimental study of the effect of automated fiber placement induced defects
on performance of composite laminates," *Composites Part A: Applied Science
and Manufacturing,* vol. 42, pp. 484-491, 2011.

[16]   J. Tierney and J. W. Gillespie, Jr., "Modeling of in situ strength development for
the thermoplastic composite tow placement process," *Journal of Composite
Materials,* vol. 40, pp. 1487-506, 2006.

[17]   M. N. Ghasemi Nejhad, R. D. Cope, and S. I. Gueceri, "Thermal analysis of in-situ thermoplastic composite tape laying," *Journal of Thermoplastic Composite Materials,* vol. 4, pp. 20-45, 1991.

[18]   M. N. Ghasemi Nejhad, "Issues related to processability during the manufacture of thermoplastic composites using on-line consolidation techniques," *Journal of Thermoplastic Composite Materials,* vol. 6, pp. 130-146, 1993.

[19]   V. Agarwal, "The role of molecular mobility in the consolidation and bonding of thermoplastic composite materials," Ph.D. 9206348, University of Delaware, United States -- Delaware, 1991.

[20]   L. J. Bastien and J. W. Gillespie, "A non-isothermal healing model for strength and toughness of fusion bonded joints of amorphous thermoplastics," *Polymer Engineering & Science,* vol. 31, pp. 1720-1730, 1991.

[21]   R. P. Wool and K. M. O'Connor, "A theory of crack healing in polymers," *Journal of Applied Physics,* vol. 52, pp. 5953-63, 1981.

[22]   R. P. Wool, "Molecular aspects of tack," *Rubber Chemistry and Technology,* vol. 57, pp. 307-319, 1984.

[23]   R. P. Wool, "Polymer entanglements," *Macromolecules,* vol. 26, pp. 1564-1569, 1993.

[24]   D. Lang, S. Barre, C. Coiffier-Colas, and H. Sibois, "Thermoplastic tape placement and continuous consolidation," NATO Research and Technology Organisation2003.

[25]   M. A. Lamontia, M. B. Gruber, S. B. Funck, B. J. Waibel, R. D. Cope, N. M. Gopez, J. F. Pratte, and N. J. Johnston, "The fabrication and performance of flat

skin stringer and honeycomb panels manufactured by a thermoplastic automated tape placement process," in *Proceedings of the 24th international SAMPE Europe conference, April 1, 2003 - April 3, 2003*, Porte de Versailles, Paris, France, 2003.

[26]   G. S. Springer, B. A. Sanders, and R. W. Tung, "Environmental effects on glass fiber reinforced polyester and vinylester composites," *Journal of Composite Materials,* vol. 14, pp. 213-32, 1980.

[27]   F. Ellyin and R. Maser, "Environmental effects on the mechanical properties of glass-fiber epoxy composite tubular specimens," *Composites Science and Technology,* vol. 64, pp. 1863-74, 2004.

[28]   Y. Sugita, C. Winkelmann, and V. La Saponara, "Environmental and chemical degradation of carbon/epoxy lap joints for aerospace applications, and effects on their mechanical performance," *Composites Science and Technology,* vol. 70, pp. 829-839, 2010.

[29]   T. Juska, "Effect of water immersion on fiber/matrix adhesion in thermoplastic composites," *Journal of Thermoplastic Composite Materials,* vol. 6, pp. 256-274, 1993.

[30]   R. Seizer and K. Friedrich, "Mechanical properties and failure behaviour of carbon fibre-reinforced polymer composites under the influence of moisture," *Composites Part A (Applied Science and Manufacturing),* vol. 28A, pp. 595-604, 1997.

[31]   A. Bismarck, M. Hofmeier, and G. Dorner, "Effect of hot water immersion on the performance of carbon reinforced unidirectional poly(ether ether ketone) (PEEK)

composites: Stress rupture under end-loaded bending," *Composites Part A (Applied Science and Manufacturing),* vol. 38, pp. 407-26, 2007.

[32]   CYTEC, *Thermoplastic composite material handbook*: Cytec Engineered Materials, 1999.

[33]   A. Lystrup and T. L. Andersen, "Autoclave consolidation of fibre composites with a high temperature thermoplastic matrix," in *AMPT '95. Advances in Materials Processing Technologies, Aug. 1995*, Switzerland, 1998, pp. 80-5.

[34]   "ASTM D3039/D3039M-08 Standard test method for tensile properties of polymer matrix composite materials," ed. West Conshohocken, PA: ASTM International, 2008.

[35]   "ASTM D5467/D5467M-97(2010) Standard test method for compressive properties of polymer matrix composite materials with unsupported gage section by shear loading," ed. West Conshohocken, PA: ASTM International, 2010.

[36]   "ASTM D5379/D5379M-05 Standard test method for shear properties of composite materials by the V-notched beam method," ed. West Conshohocken, PA: ASTM International, 2005.

[37]   "ASTM D5766/D5766M-11 Standard test method for open-hole tensile strength of polymer matrix composite laminates," ed. West Conshohocken, PA: ASTM International, 2011.

[38]   "ASTM D6484/D6484M-09 Standard test method for open-hole compressive strength of polymer matrix composite laminates ", ed. West Conshohocken, PA: ASTM International, 2009.

[39]   R. K. Roy, *Design of experiments using the Taguchi approach: 16 steps to product and process improvement*: Wiley, 2001.

[40]   "ASTM D2344/D2344M-00(2006) Standard test method for short-beam strength of polymer matrix composite materials and their laminates," ed. West Conshohocken, PA: ASTM International, 2006.

[41]   M. Cirino and R. Byron Pipes, "In-situ consolidation for the thermoplastic composite ring—residual stress state," *Composites Manufacturing,* vol. 2, pp. 105-113, 1991.

[42]   "ASTM D5868-01(2008) Standard test method for lap shear adhesive for fiber reinforced plastic (FRP)," ed. West Conshohocken, PA: ASTM International, 2008.

[43]   F. Desplentere, S. V. Lomov, D. L. Woerdeman, I. Verpoest, M. Wevers, and A. Bogdanovich, "Micro-CT characterization of variability in 3D textile architecture," *Composites Science and Technology,* vol. 65, pp. 1920-1930, 2005.

[44]   P. J. Schilling, B. P. R. Karedla, A. K. Tatiparthi, M. A. Verges, and P. D. Herrington, "X-ray computed microtomography of internal damage in fiber reinforced polymer matrix composites," *Composites Science and Technology,* vol. 65, pp. 2071-2078, 2005.

[45]   J. S. U. Schell, M. Renggli, G. H. van Lenthe, R. Muller, and P. Ermanni, "Micro-computed tomography determination of glass fibre reinforced polymer meso-structure," *Composites Science and Technology,* vol. 66, pp. 2016-22, 2006.

[46]   P. Badel, E. V. Salle, E. Maire, and P. Boisse, "Simulation and tomography analysis of textile composite reinforcement deformation at the mesoscopic scale," *International Journal of Material Forming,* vol. 2, pp. 189-192, 2009.

[47]   L. P. Djukic, I. Herszberg, W. R. Walsh, G. A. Schoeppner, and B. Gangadhara Prusty, "Contrast enhancement in visualisation of woven composite architecture using a MicroCT Scanner. Part 2: Tow and preform coatings," *Composites Part A: Applied Science and Manufacturing,* vol. 40, pp. 1870-1879, 2009.

[48]   T. Centea and P. Hubert, "Measuring the impregnation of an out-of-autoclave prepreg by micro-CT," *Composites Science and Technology,* vol. 71, pp. 593-9, 2011.

[49]   "ASTM D5229/D5229M-92(2010) Standard test method for moisture absorption properties and equilibrium conditioning of polymer matrix composite materials," ed. West Conshohocken, PA: ASTM International, 2010.

[50]   "ASTM D5573-99(2005) Standard practice for classifying failure modes in fiber-reinforced-plastic (FRP) joints," ed. West Conshohocken, PA: ASTM International, 2005.

[51]   C. A. Mahieux, D. Lehmann, and A. desLigneris, "Experimental determination of the effects of industrial oil immersion on polymer-based composites," *Polymer Testing,* vol. 21, pp. 751-6, 2002.

[52]   D. M. Maguire, "Joining thermoplastic composites," *SAMPE Journal,* vol. 25, pp. 11-14, 1989.

[53]   E. M. Silverman and R. A. Griese, "Joining methods for graphite/peek thermoplastic composites," *SAMPE Journal,* vol. 25, pp. 34-38, 1989.

[54]   X. R. Xiao, S. V. Hoa, and K. N. Street, "Repair of thermoplastic composite structures by fusion bonding," in *35th International SAMPE Symposium and Exhibition - Advanced Materials: the Challenge for the Next Decade. Part 2, April 2, 1990 - April 5, 1990*, Anaheim, CA, USA, 1990, pp. 37-45.